NWC TP 5110

HIGH-VELOCITY IMPACT OF STEEL SPHERES ON METALLIC TARGETS

by

Werner Goldsmith
University of California, Berkeley
and
Stephen A. Finnegan
Kenneth I. Rinehart
Research Department

ABSTRACT. A study was made of the penetration, perforation, and fragmentation of 0.05 to 0.25-inch-thick 2024 aluminum, SAE 1020, and 4130 steel alloy plates impacted normally by 0.125-, 0.25-, and 0.375-inch-diameter AISI 52-100 hard steel spheres at velocities from 2,800 to 8,800 fps. The drop in projectile velocity was found to decrease just above the ballistic limit, then steadily rise with increasing initial bullet speed in all target-projectile configurations. The first trend was predicted by a relation based on a simple momentum balance, whereas a more precise analysis provided reasonable correspondence with the data over the entire velocity range. Strain gage results showed a decrease of dishing relative to radial target motion with increasing impact velocity. Displacement-time curves were constructed using measured initial and terminal projectile velocities, fragment dimensions, and Kerr cell records. Force histories of the projectiles were then computed from these data using an empirical relation developed previously. Peak forces obtained were in reasonable agreement with calculations from a triangular impulse of the proper duration and of magnitude equal to the measured change in momentum.

NAVAL WEAPONS CENTER
CHINA LAKE, CALIFORNIA * MAY 1971

NAVAL WEAPONS CENTER
AN ACTIVITY OF THE NAVAL MATERIAL COMMAND

W. J. Moran, RADM, USN ..... Commander
H. G. Wilson ..... Technical Director

FOREWORD

The material in this report represents part of a continuing research program at the Naval Weapons Center in support of explosive ordnance problems.

These studies were supported by funds under the Naval Air Systems Command Task Assignment A1503500-2168-1F17353501 and were performed jointly by Dr. Werner Goldsmith, Professor of Mechanical Engineering at the University of California, Berkeley, and by Research Department personnel.

Because of the continuing nature of the explosive ordnance studies being made at the Center, refinements and modifications may later be made in the methods and measurements discussed.

Released by
JOHN PEARSON, *Head*
Detonation Physics Division
1 March 1971

Under authority of
HUGH W. HUNTER, *Head*
Research Department

NWC Technical Publication 5110

Published by ..... Research Department
Collation ..... Cover, 29 leaves, DD Form 1473, abstract cards
First printing ..... 205 unnumbered copies
Security classification ..... UNCLASSIFIED

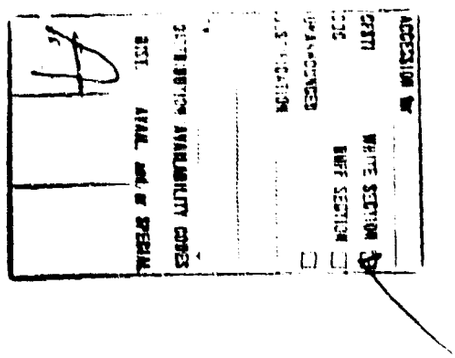

DOCUMENT CONTROL DATA - R & D

Naval Weapons Center
China Lake, California 93555

UNCLASSIFIED

HIGH-VELOCITY IMPACT OF STEEL SPHERES ON METALLIC TARGETS

Research Report

Werner Goldsmith, Stephen A. Finnegan, Kenneth I. Rinehart

May 1971

56

36

NWC TP 5110

NAVAIR A350350D-216B-1F17353501

APPROVED FOR PUBLIC RELEASE: DISTRIBUTION UNLIMITED

Naval Air Systems Command
Department of the Navy
Washington, D. C. 20360

A study was made of the penetration, perforation, and fragmentation of 0.05 to 0.25-inch-thick 2024 aluminum, SAE 1020, and 4130 steel alloy plates impacted normally by 0.125-, 0.25-, and 0.375-inch-diameter AISI 52-100 hard steel spheres at velocities from 2,800 to 8,800 fps. The drop in projectile velocity was found to decrease just above the ballistic limit, then steadily rise with increasing initial bullet speed in all target-projectile configurations. The first trend was predicted by a relation based on a simple momentum balance, whereas a more precise analysis provided reasonable correspondence with the data over the entire velocity range. Strain gage results showed a decrease of dishing relative to radial target motion with increasing impact velocity. Displacement-time curves were constructed using measured initial and terminal projectile velocities, fragment dimensions, and Kerr cell records. Force histories of the projectiles were then computed from these data using an empirical relation developed previously. Peak forces obtained were in reasonable agreement with calculations from a triangular impulse of the proper duration and of magnitude equal to the measured change in momentum.

14 KEY WORDS	LINK A		LINK B		LINK C	
	ROLE	WT	ROLE	WT	ROLE	WT
Impact						
Penetration						
Perforation						
Target behavior						
Kerr-cell photography						

CONTENTS

Figures: (Contd.)

Tables:

INTRODUCTION

Physical Processes

In the usual cases of ballistic impact, the project will either embed itself in the target (penetration) or else pierce the target completely (perforation). The resistance to penetration or perforation by projectiles is a difficult problem to analyze because of the variety of simultaneous physical processes that can be activated. These processes invariably include elastic, plastic, or viscoelastic deformation of both projectile and target, and result in the formation of a crater or hole. With increasing collision speed, fracture, comminution, burning or even explosion of the participating solids may also occur, depending on their geometries, physical properties, and relative velocity, (Ref. 1).

The complexity of these phenomena has prevented the construction of more comprehensive models of the perforation or penetration processes that would incorporate all variables present and predict the final state simply from the initial collision conditions. Analyses have been generally confined to simplified physical situations involving only one perforation mechanism, usually assumed a priori, or else invoke unrealistic hypotheses such as a constant projectile velocity during perforation. There has been no systematic attempt to catalog the major phenomena occurring in the penetration and perforation of plates as a function of impact velocity so that analytical models could be matched with the appropriate ranges of velocity. The present report describes the results of an investigation concerned with isolating major phenomena involved in the penetration and perforation of thin plates by spherical projectiles at and above ordnance velocities.

Projectile impact problems can be categorized in terms of impact velocities and major phenomenon encountered. In the range below 10,000 fps, collisions are primarily elastic at very low velocities; include plastic deformation of the target and initiate local fracturing at intermediate velocities; result in failure or perforation of the target at somewhat higher velocities and, depending on the nature of the colliding elements, produce extensive breakup of the target at high velocities. Various degrees of projectile deformation or fracturing may also occur depending on its relative hardness, strength, and geometry. In the hypervelocity range, above 10,000 fps, the impacting elements are usually treated as fluids and the collision is analyzed by methods of hydrodynamics including shock heating (Ref. 2). At even more extreme velocities as encountered in meteoritic impact, pulverization, vaporization, phase transitions, and even impact explosions have been observed or hypothesized and simplified analyses attempted (Ref. 3).

Elastic Impact

Impact on elastic plates of infinite extent was first theoretically described by Boussinesq' (Ref. 4) whose solution was adapted for an arbitrarily specified triangular forcing function concentrated at the origin; the same loading was also applied to clamped circular plates by means of a normal mode technique (Ref. 5). Good qualitative agreement was observed between the predictions and the results of corresponding experiments. Other results for a rectangular plate (Ref. 6) and for an infinite plate (Ref. 7) include the indentation process of the spherical striker and determine the contact force history as part of the solution.

Plastic Impact

For situations involving permanent deformations, analytical solutions generally require the adoption of unrealistic physical conditions. Thus, the relations for the impact of a rigid cylinder on a rigid/perfectly plastic circular plate based on the Tresca yield condition invokes a condition of constant projectile velocity (Ref. 8). Another study of this problem (Ref. 9) involving a general piecewise linear yield condition with a single travelling yield hinge provided a compatible solution only for a constant transverse velocity step input at the origin, the radial velocity of the yield hinge being proportional to the square root of time. In addition to the lack of a well-posed problem for this case (leaving one constant of integration unspecified), the solution for the corresponding work-hardening case led to a complete contradiction that implies the requirement of either a drastically different model of the plate deformation or else a relaxation or alteration of the fundamental laws of plasticity for dynamic situations.

A solution has been derived for the impact of a projectile on a clamped viscoplastic plate governed by the Mises yield condition that includes the interaction of the colliding objects, the contact force or projectile motion not being specified a priori (Ref. 10). The inherent nonlinearity in this analysis was obviated by a linearization process employed previously (Ref. 11); these results were also applied to the case of large plate deflections (Ref. 12). An approximation to the solution of Ref. 10 was found to be in good agreement with experimental results obtained by impacts at velocities up to 1,950 fps of 0.454-inch-diameter cylindrical projectiles on 0.25-inch-thick mild steel plates, which have been clamped on a 4-inch-diameter.

Perforation Models

Numerous physical and analytical models have been proposed to explain the various observed perforation modes which include plug formation by shearing, dishing of the target with petal formation, ductile hole enlargement, fragmentation or spalling (Ref. 1,5,13). Theoretical descriptions of the process generally concentrate on only one mode of plate failure—ordinarily without the accompanying effects of additional plate

deformation remote from the contact point—and then usually under further restrictive hypotheses of a specific target/projectile combination within a limited velocity range. Several analyses using an energy balance and based on the concept of an expanding hole calculate the work required for perforation of a plate (Ref. 14,15,16). Simple energy and momentum balances were used, along with an empirical knowledge of the minimum perforation velocity, to calculate residual projectile velocities for a plugging perforation process at normal and oblique impacts (Ref. 17). This solution was found to correlate well with experimental data up to impact velocities of 4,000 fps. The conservation of momentum principle was applied within a region proximate to the contact point to calculate projectile velocities when the deformation pattern within this domain was assumed a priori (Ref. 18,19,20). A solution has also been obtained for a plug-type of failure of a viscous model considering only the vertical shearing stresses (Ref. 21,22).

In a recent investigation (Ref. 23), the normal perforation of metallic plates by small-caliber lead projectiles was analyzed by dividing the process into two parts: (a) initial indentation without plug formation during which the inertial force and compressive resistance of the target material are active and where the effective mass of the projectile is assumed to increase by the amount of the target material displaced, and (b) the plugging process where only the shearing force acts and there is no change of the effective projectile mass. The diameter and thickness of the sheared plug, both a priori unknown quantities, must be either hypothesized or determined from test information. Friction and heating are neglected and the plugging phase is completely absent during ductile perforation. The relevant analytical expressions and definitions are presented in Appendix A together with a sketch of the process. Excellent correspondence was obtained between the predictions of this theory and experimental data.

PREVIOUS STUDIES

While numerous experiments have involved impact on elastic plates (Ref. 2,24,25), there have been virtually no investigations concerned with the large plastic deformations of targets subjected to collisions. Perforation tests have sometimes been concerned with the measurement of residual projectile velocity (Ref. 5,17,23,26,27), with the frictional forces developed during armor penetration (Ref. 29,30), and with elastic wave effects produced in remote regions (Ref. 31).

Two earlier analytical and experimental studies involving both spherical and cylindro-conical steel bullets striking targets composed of either aluminum or steel[1] (Ref. 1,5) served as the basis for the present

[1] Calder, C.A. and W. Goldsmith. "Plastic Deformation and Perforation of Thin Plates Resulting From Projectile Impact" and C. A. Calder, J. M. Kelly, and W. Goldsmith, "Projectile Impact on an Infinite Viscoplastic Plate" both to appear (1971) in INT J SOLIDS STRUC.

study. The domains of interest in these tests were the regimes of (a) substantially elastic impact, (b) that of perforation at minimal velocities, i.e., just above the ballistic limit, (c) the perforation domain from incipient piercing to the limit permitted by the pneumatic propulsion equipment available, about 1,500 fps for a 0.25-inch-diameter steel sphere, and (d) that involving substantial plastic deformation without perforation. Targets consisted of 0.05-inch-thick steel and aluminum plates and 0.125-inch-thick aluminum plates. The principal parameters determined experimentally were the initial and terminal velocity of the projectile, the position history of projectile and target by means of a high-speed framing camera, elastic wave propagation in the target outside the plastically deformed region by means of strain gages, and the final shape of the target evaluated by a profilometer. The following is a summary of previous results of normal impact tests involving 0.5-inch and 0.25-inch-diameter spherical or cylindro-conical steel projectiles against 0.05-inch-thick 2024-0 and 1100-H14 aluminum alloy plates and 0.048-inch-thick mild steel, at impact velocities of 75 to 1,289 fps, up to and including perforation.

Sub-Perforation Impact

At impact velocities below perforation, a simplified large-deflection solution for the final central deflection of a rigid/plastic linearly work-hardening plate agreed well with experimental data for soft aluminum. A more rigorous rigid/viscoplastic solution, based only on bending grossly overpredicted permanent deflections in the steel plates, indicating the presence of large membrane effects. The 0.5-inch-diameter spherical projectile produced permanent deflections in the aluminum targets that increased almost linearly with impact velocity, and were located radially within about a 2-inch radius from the impact point. Plate deflections were equal for clamped and freely suspended aluminum plates indicating that edge reflections were not significant in these tests. The peak force occurred early in impact, reaching a value of 1,400 pounds at 83 μsec for a 0.5-inch-diameter sphere striking a 2024-0 target with a contact time of 430 μsec at a velocity of 397 fps, just below the ballistic limit. Projectile rebound energy and elastic plate energy were each found to be less than 1% of the initial kinetic energy. At least 95% of the initial kinetic energy was believed to be absorbed by plastic deformation of the plate.

Perforation Processes

Various perforation theories compared poorly with experimental data at low velocities, where plate motion and plastic deformations adjacent to the contact surface are large and extend considerably outward from the contact area, but correlation improved as impact velocities increased and deformations localized about the crater edge as assumed by these theories. Perforation occurred by plugging and dishing or by petalling and dishing for a sphere or a pointed projectile, respectively. The plug diameter

was smaller than that of the sphere and increased in size with increasing velocity. For a 0.5-inch-diameter spherical or pointed projectile perforating a 0.050-inch 2024-0 aluminum plate at an impact velocity of 497 or 301 fps, respectively, a peak force of 1,500 pounds at 45 μsec or 650 pounds at 95 μsec is produced with a total contact duration of 175 or 300 μsec.

Additionally, in the 2024-0 aluminum targets, greater than 2% peak strains were found 0.5-inch from the impact center that propagated outward at about 8,800 fps at all impact velocities. This was the identical velocity found for the radial growth of the central plastic zone out to a 1.5-inch radius. Target boundaries had no effect on these quantities providing they were not inside the deformed zone.

CURRENT INVESTIGATION

This investigation was intended to extend the domain of interest to initial velocities up to 10,000 fps, and to examine the effect of material properties on the perforation process by striking two different steels and three grades of aluminum alloy with four different thicknesses. High-speed photography, strain gage data, initial and terminal projectile velocities, and terminal target profiles were obtained. The propulsion device and the camera technique differed significantly from the system used previously.

EXPERIMENTAL ARRANGEMENT AND PROCEDURE

A schematic of the experimental arrangement is shown in Fig. 1, and a photograph of the setup is presented in Fig. 2. The propulsion device (Ref. 32) consisted of a smooth-bore, 50 caliber powder gun fitted with a vented guide section that was located in an evacuated environment. Velocities were measured in the gun barrel with a photo diode system coupled to an interval counter. Projectiles consisted of 0.25-inch and 0.375-inch-diameter AISI 52-100 hard steel balls, plus a few 0.125-inch-diameter steel or 0.25-inch-diameter 2024-T3 aluminum balls. A 0.25-inch-diameter steel cylindro-conical projectile was also fired, but it proved to be too unstable in flight to yield reproducible impacts. Projectiles were fitted into 0.5-inch-diameter polycarbonate sabots designed to fly apart after leaving the gun barrel. Sabot pieces and fragment debris were trapped downrange by a series of thick steel plates, each containing a central hole to allow the projectile to pass through. Projectile impact and perforation velocities at the target were measured with two inductive coil systems (Ref. 33). Figure 3 shows the target arrangement.

Baldwin-Lima Hamilton SR-4, Type FAP-12-12 foil gages with a gage factor of either 2.05 or 2.08 and a resistance of 120 ohms were mounted with Eastman 910 cement on both the impact and distal side of selected

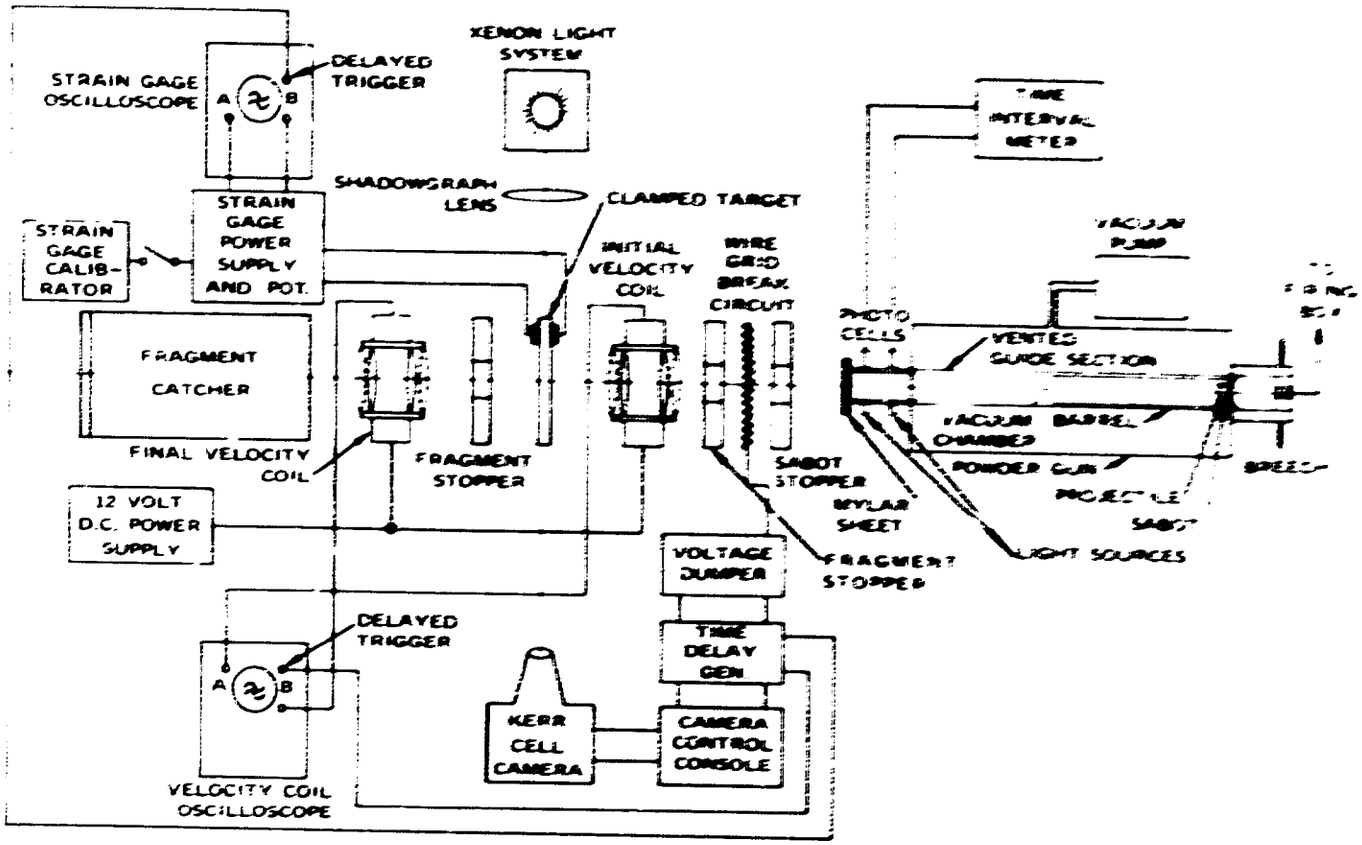

FIG. 1. Schematic of Experimental Arrangement.

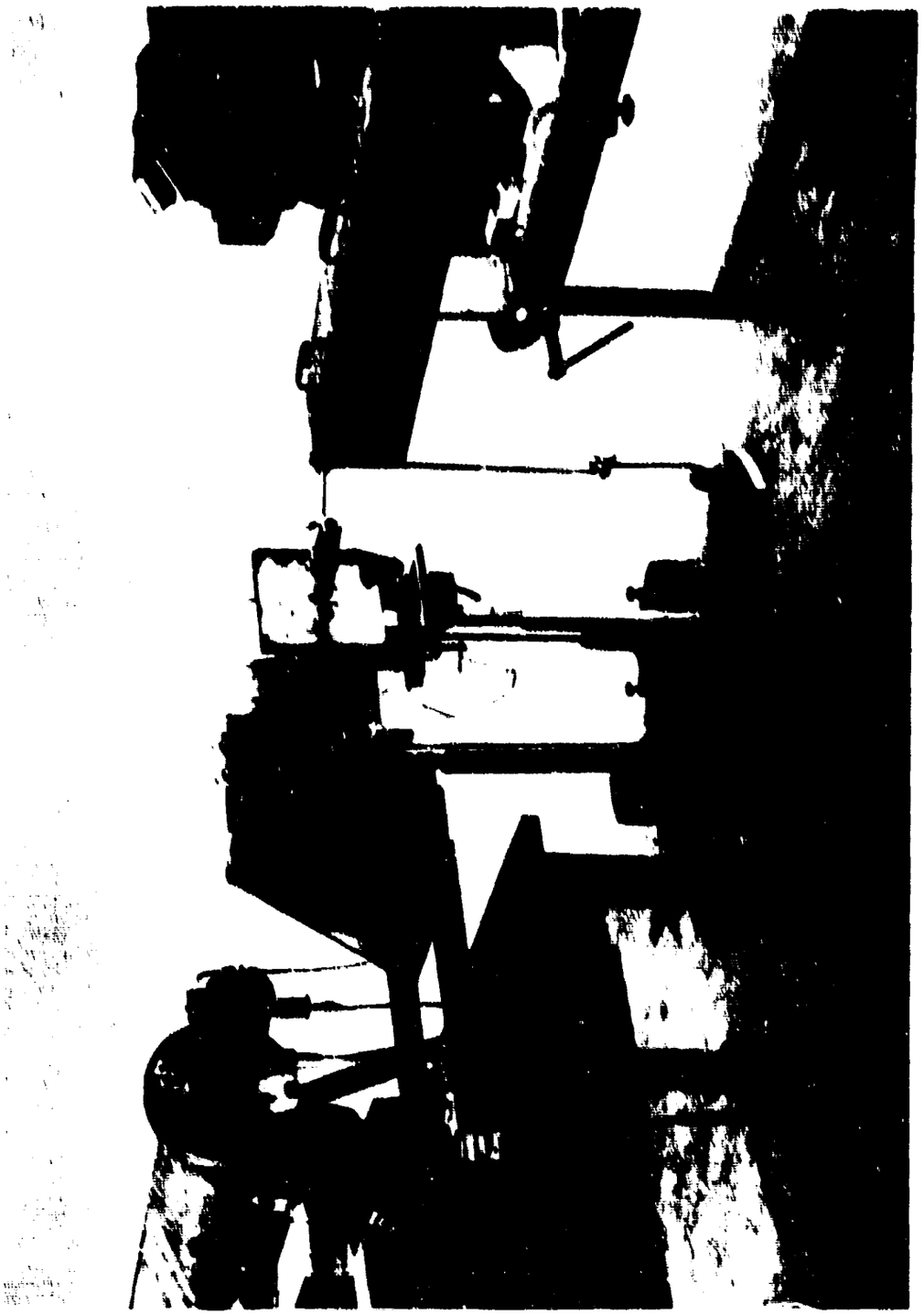

FIG. 2. Photograph of Setup.

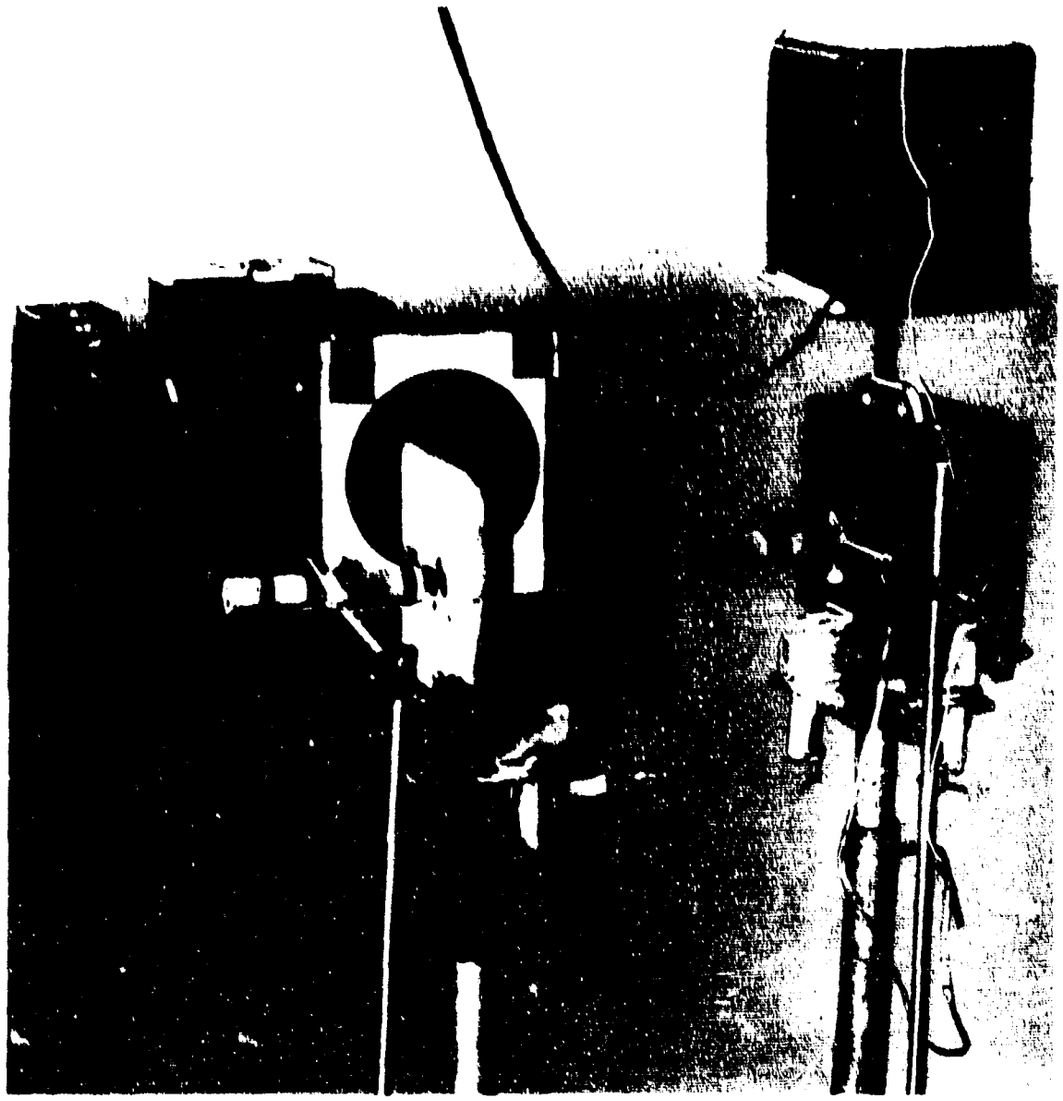

FIG. 3. Target Arrangement.

plates at specified positions from the impact point, oriented both in the radial and circumferential directions. These gages were energized by a 12-volt battery and were included with a 120-ohm ballast resistor in a potentiometric circuit whose output was displayed on an oscilloscope. Prior to each test, all active strain gages were calibrated by recording the deflection produced by each upon inclusion in the circuit of a series of shunt resistances ranging from ten thousand to one million ohms.

The impact process was photographed with a six-frame Beckman-Whitley KFC-600 Kerr cell camera using a focussing shadowgraph backlighting scheme (Ref. 34, 36). A wire grid "break circuit" in the path of the projectile and delay generator served as a common trigger for oscilloscopes recording the strain gage and velocity coil signals. The Tektronix 555 oscilloscopes used Type B or C preamplifiers with a bandpass exhibiting a drop of three decibels at ten megahertz.

Targets consisted of 12- or 8-inch-square plates of the following materials:

0.25-inch-thick SAE 4130 alloy steel armor, quenched and tempered to 40 R_C
0.25-inch-thick SAE 1020 large-grained mild steel
0.25-inch-thick SAE 1020 small-grained mild steel
0.25-inch-thick 2024-T4 aluminum
0.125-inch-thick 2024-T3 aluminum
0.062-inch-thick SAE 1020 small-grained mild steel
0.05-inch-thick 2024-0 aluminum
0.05-inch-thick 2024-T3 aluminum

Targets were frequently used several times, especially when instrumented with strain gages. They were clamped at two points of a single edge onto a rigid stand and were usually centered in the projectile path. In the case of multiple impacts, plates were positioned to remove bulges from previous shots from the camera's field of view. In no case was the impact point closer than 5 inches from an edge. A set of dividers with the points spaced 1 1/2 inches apart was placed in the vertical plane below the projectile path to provide an accurate distance reference on the photographs.

Four separate types of runs were performed: (a) camera data runs, (b) strain gage data runs, (c) fragment recovery runs, and (d) ballistic limit determinations. Unfortunately, strain gage information and photographs of the perforation process could not be obtained together as transient electrical fields produced by the high voltage condenser discharge in the camera system totally obscured the strain gage signal. However, this disturbance was usually not so large as to completely erase the oscilloscopic traces of the velocity tube signal. In consequence, projectile velocities were obtained in almost all of the runs of types (a) and (b). Fragments were also recovered in additional tests to provide supplemental information for the determination of the history of the contact force.

Representative targets were sectioned to provide a contour of the deformation and the crater, and crater diameters were measured for most of the tests. Static tensile tests were conducted on materials not previously examined (Ref. 35) to define their mechanical state. Metallographic tests on the target plates were also accomplished by standard methods.

DATA REDUCTION PROCESS

In general, it was not possible to obtain an adequate photographic record of the perforation process for a given projectile-target configuration and a specified initial velocity with a single round, particularly since the time delays at the higher velocities required accuracy to a fraction of a microsecond that could not be achieved with the available equipment. It was therefore necessary to combine the camera data from a number of identical (or nearly identical) rounds by interpolating the position of either the projectile, the air shock wave or the plate bulge in order to form a complete displacement history of the bullet. The flash produced by contact with a target, particularly at high-impact velocities, frequently obscured the projectile position on the impact side, and its location had to be deduced from the frontal bulge formed during perforation. This led to an uncertainty in its position, represented by two parallel lines with a separation equal to the target thickness and a slope equal to the terminal velocity, with the extremes denoting the formation of a cap or plug of zero thickness of that of the full target, respectively. Greater precision required a knowledge of the actual plug thickness produced, and additional tests were made to obtain this information. Considerable uncertainty in plug thickness exists for initial velocities in excess of 4,000 fps in the aluminum and thin steel targets and above about 6,500 fps for the thick steel plates due to severe breakup. In consequence, results were extrapolated to the higher velocities as shown in Fig. 4.

Position-time curves of the projectile were drawn from the independently measured initial and terminal velocity, v_i and v_f, respectively, and the interpolated camera data. The position of the projectile or that of the shock wave in one of the frames could almost invariably be matched with that in a photograph from another set. The curves were drawn in tangent to the slopes established from the velocity data at the points of initial and terminal contact, respectively. Initial contact could nearly always be determined with reasonable precision from the appearance of a flash. Perforation was considered to be complete when the equator of the sphere just traversed the distal side of the plate at a distance equal to the target thickness plus one-half the ball diameter from the position of initial contact on the plot. The corresponding perforation time is then determined by the intersection of this position with a line parallel to the distal plate face locus and at a distance equal to the cap thickness. This process is shown in Fig. 5: (a) denotes

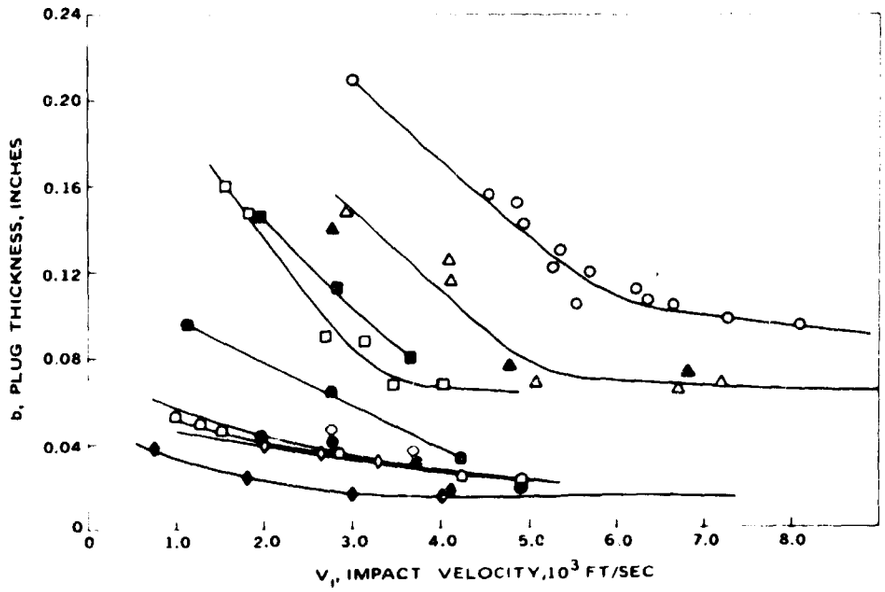

SYMBOL	TARGET	STEEL PROJECTILE DIAMETER
○	0.250 4130 STEEL ARMOR	0.250
△	0.250 1020 STEEL (LARGE GRAINED)	0.250
▲	0.250 1020 STEEL (SMALL GRAINED)	0.250
□	0.250 2024-T4 ALUMINUM	0.250
■	0.250 2024-T4 ALUMINUM	0.375
●	0.125 2024-T3 ALUMINUM	0.250
⌂	0.0625 1020 STEEL (SMALL GRAINED)	0.250
●	0.0625 1020 STEEL (SMALL GRAINED)	0.375
◊	0.050 2024-T3 ALUMINUM	0.250
◆	0.050 2024-0 ALUMINUM	0.250
◌	0.050 2024-T3 ALUMINUM	0.375

FIG. 4. Measured and Extrapolated Plug Thickness as a Function of Impact Velocity.

the initial contact, at time t_o, with the position, s, relative to the plate center reasonably accurately ascertained from the photograph but also in general accord with the relation $s(t_o) = -[2R+\frac{1}{2}h_o]$ where h_o is the target thickness and R the sphere radius, (b) an intermediate point during perforation whose right-hand limit is observed from the bulge, and whose left-hand limit is shifted by the amount of the original target thickness, so that the difference between b_1 and h_o is the uncertainty in the location of the front of the projectile, and (c) completion of perforation with the quantity b_2 equal to the measured or estimated cap thickness. In some instances, more than one plug thickness was considered resulting in more than one displacement-time curve for the same

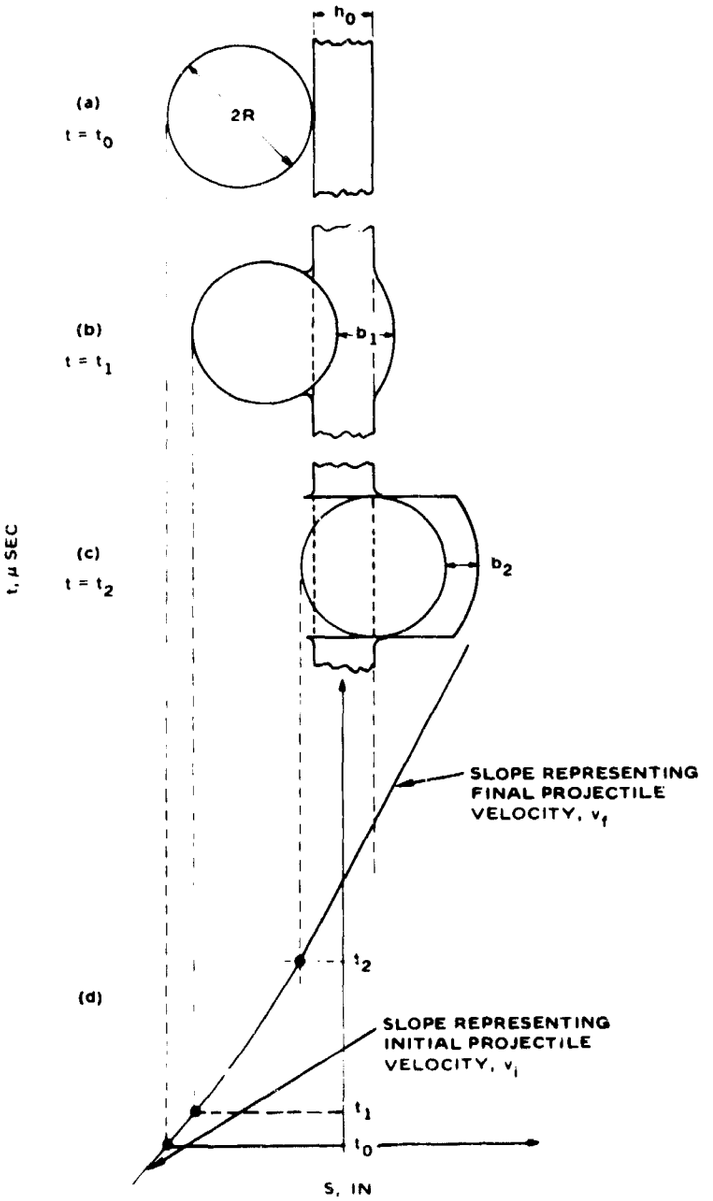

FIG. 5. Schematic of Perforation Process: (a) initial contact, (b) partial perforation, (c) complete perforation, and (d) projectile displacement-time curve.

initial and terminal velocities, with the most appropriate chosen for further analysis. Positions beyond t_2 are presented in the results to give some indication of the scatter of data.

In spite of these constraints, there still existed some freedom in the actual construction of the bullet trajectories; these were resolved by placing the maximum curvature in an early segment of these plots. This is based upon the applicability of Newton's law to the center of mass of the projectile, whether intact or in fragments, so that the contact force F is proportional to the acceleration $\ddot{y}$, i.e., $F = m_o\ddot{y}(t)$, where m_o is the mass of the bullet and y is the bullet displacement. On the basis of previous tests (Ref. 5,30) and expectation, the shape of the force-time curves should peak during the first half of the contact duration, requiring the construction outlined above. The fixed slopes at the established initial and terminal contact positions also determine two absolute bounds for the position of the projectile path.

In most cases, the plug thickness data yielded information consistent with the other measurements so that the uncertainties in the location and curvature of the position-time curves are small. However, in a few instances, the use of such thicknesses would have violated the other constraints cited above. In such cases, the plug thickness results were either modified or disregarded since they represented the least reliable data obtained during the experiments.

The final displacement-time diagrams constructed in this fashion, $y = f(t)$, were then fitted to the three-parameter empirical equations

$$y(\pi\xi) = \frac{A}{B^4}e^{-B\pi\xi}\left[B^2\pi^2\xi^2 + 4B\pi\xi + 6\right] + \left[v_i + \frac{2A}{B^3}\right]\pi\xi + D;\ v_f = 0 \qquad (1)$$

for the permanent dent (nonperforation) and

$$y(\pi\xi) = \frac{B(v_i - v_f)e^{-B\pi\xi}}{2(B^2+4)(e^{-\pi B}-1)}\left(B^2\sin^2\pi\xi + 2B\sin 2\pi\xi + 2\cos 2\pi\xi + 4 + \frac{8}{B^2}\right) + \frac{(v_i e^{-\pi B} - v_f)\pi\xi}{e^{-\pi B}-1} + D \qquad (2)$$

for the perforation case, respectively. Here, the quantities A, B, and D are to be evaluated for each run from the best fit of each curve, with the parameter $\xi = (t/\tau)$ as nondimensional time, and τ as the observation time or the duration of contact for the two cases, respectively. Equations (1) and (2) are obtained by integration from the assumed acceleration relations for the two cases.

$$\ddot{y}(\pi\xi) = A\pi^2\xi^2 e^{-B\pi\xi} \tag{3}$$

and

$$\ddot{y}(\pi\xi) = Ae^{-B\pi\xi}\sin^2\pi\xi \tag{4}$$

respectively, that had previously been found to yield suitable force-time curves for projectiles striking metallic targets (Ref. 1,30). Application of Newton's law then yields the force from either Eq. (3) or Eq. (4). A computer solution was employed to calculate the best values of the constants from the experimental formation.

Strain-time data was obtained from the known oscilloscopic sweep speeds and the calibration involving the use of a shunt resistance R_s. Strain ϵ produced by the use of such a resistance is given by the expression

$$\epsilon = \frac{1}{G.F.\left[1 + \frac{R_s}{R_g}\right]} \tag{5}$$

where G.F is the gage factor and R_g the gage resistance. For a fixed gage voltage, the excursion on the oscilloscope thus corresponds to a definite strain that is linearly related to all other deflections.

Corresponding points of deflection on the oscilloscopic traces of the velocity tube signals were employed to calculate the projectile speed. Although high-frequency noise was found on all records of the second tube when the arc lights were flashed, it was generally possible to isolate the signal unambiguously.

RESULTS

Two typical sequences for a projectile perforating a thin and thick aluminum target at low velocity are shown in Fig. 6 and 7, respectively; both represent the composite from a number of runs. The perforation of a thin target clearly occurs by means of a plugging process while for the thicker target, petalling can be observed in the later stages. Figure 8 presents the perforation of a 0.25-inch-thick plate by a 0.25-inch-diameter steel sphere initially travelling at a velocity of 8,650 fps. Another set of photographs depicting the embedment of a projectile is shown in Fig. 9. Average values of the initial velocity, the velocity drop, the inner crater diameter and the crater depth, for all primary runs are presented in Table 1.

Representative strain gage records for these various phenomena are shown in Fig. 10 through 15, corresponding to the perforation of thin and thick targets and penetration (embedment) of a thick target as

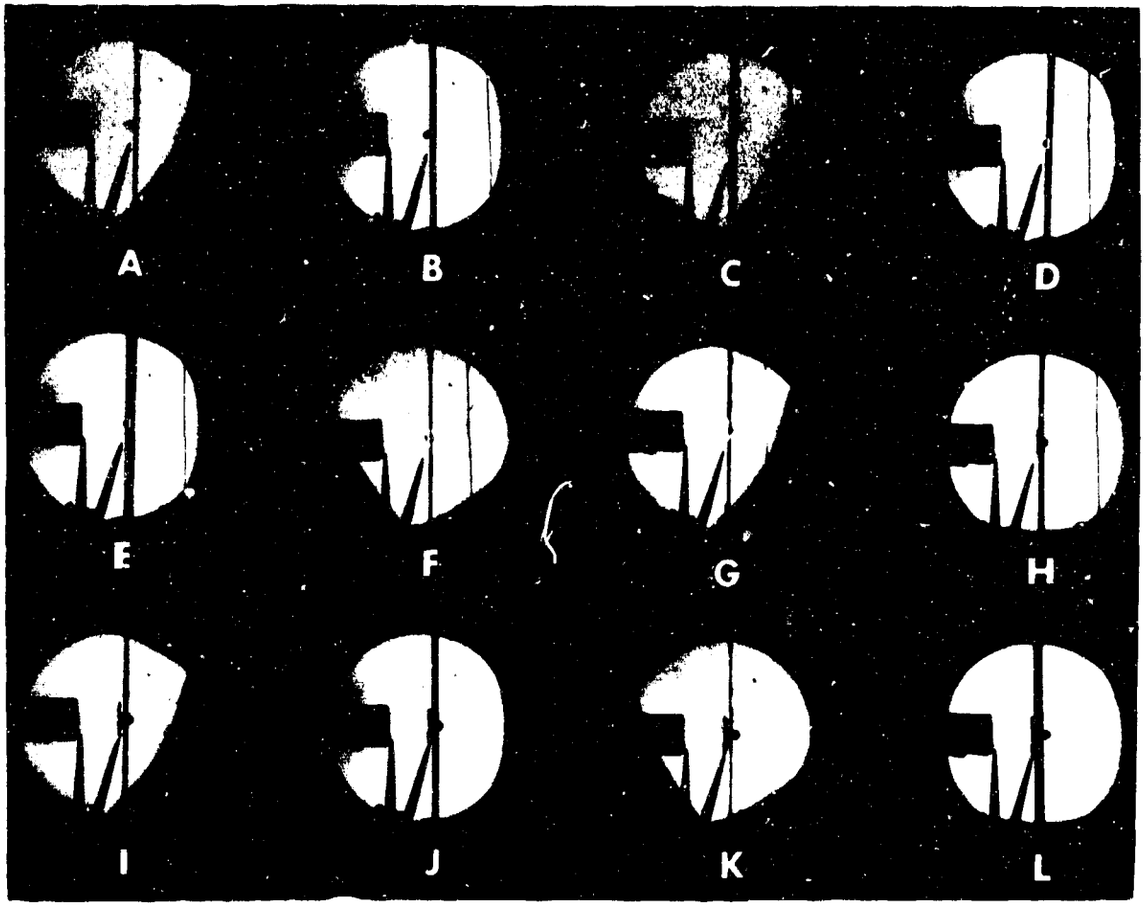

FIG. 6. Photographic Sequence. Perforation of a 0.05-inch-thick 2024-T3 aluminum plate by a 0.25-inch-diameter steel sphere at an initial velocity of 2,800 fps. Time of each frame in microseconds t, relative to initial contact given by t = -2.9; -1.1; -0.2; 0.6; 1.4; 2.9; 4.3; 5.9; 7.6; 8.8; 11; and 13 for frames (A) through (L), respectively.

measured by strain gages aligned in the longitudinal (L) and transverse (T) directions. In all instances, gages labeled 5 and 6 are located at the same distance from the impact point and oriented in the same manner, but are mounted on the impact and distal side of the plate, respectively. All such pairs were recorded during the same test.

All strain gage records show the presence of an initial symmetric component of strain followed by an antisymmetric (bending) component generated by the impact. Table 1 summarizes these results for the various configurations with the position of the gages from the impact point indicated. The table also includes the data from runs designed to study

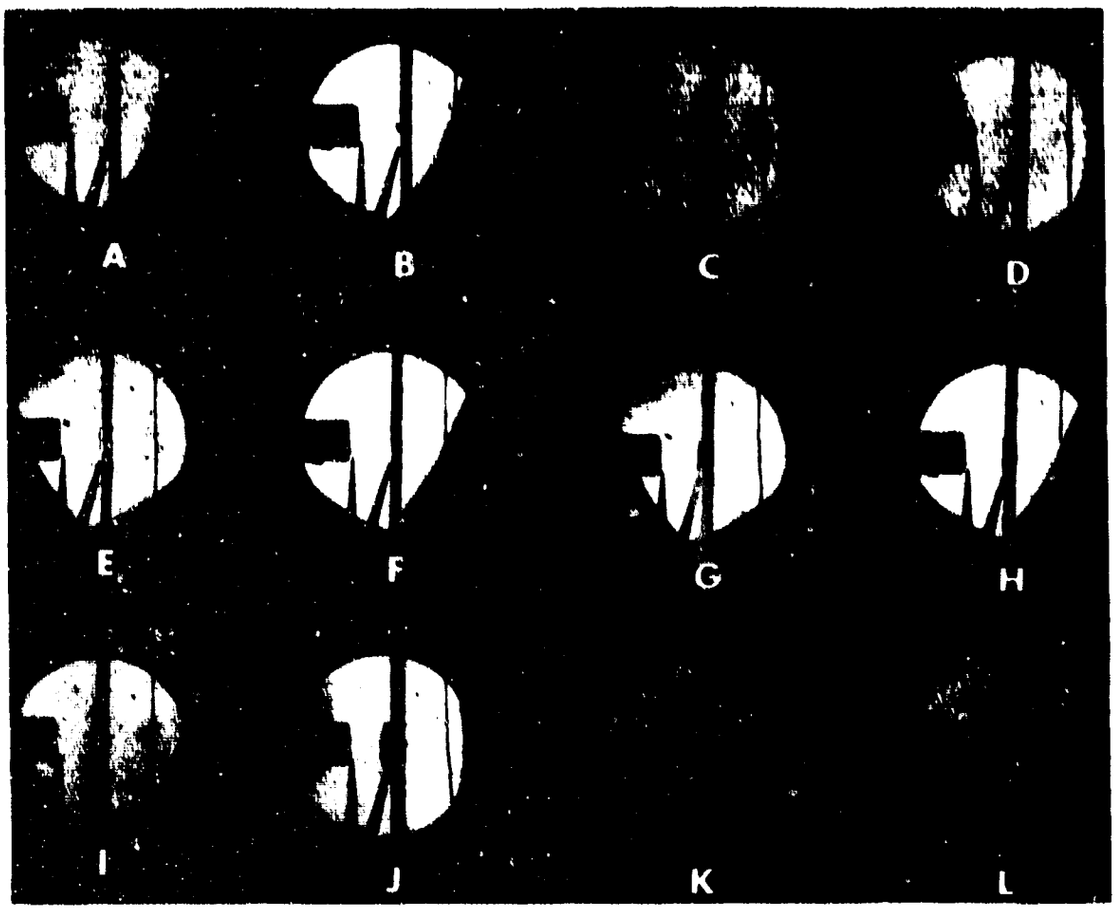

FIG. 7. Photographic Sequence. Perforation of a 0.25-inch-thick 2024-T4 aluminum plate by a 0.25-inch-diameter steel sphere at an initial velocity of 2,850 fps. Time of each frame in microseconds t, relative to initial contact given by t = -0.7; 0.6; 1.4; 2.6; 3.6; 4.7; 5.7; 7.8; 10.8; 15.0; 18.7; and 21.5 for frames (A) through (L), respectively.

the effect of variation in the initial velocity of the 0.25-inch-diameter steel projectile on the strain in the radial direction in 0.25-inch-thick armor plate at a position 1.5 inches from the impact point. Furthermore, it contains results involving the variation in the peak radial symmetric and bending strains as a function of distance from the impact point for a 0.25-inch-diameter steel projectile striking a 0.25-inch-thick mild steel target at a velocity of about 4,300 fps.

The first of these special studies indicates that the maximum symmetric strain at a given position decreases slightly with impact velocity

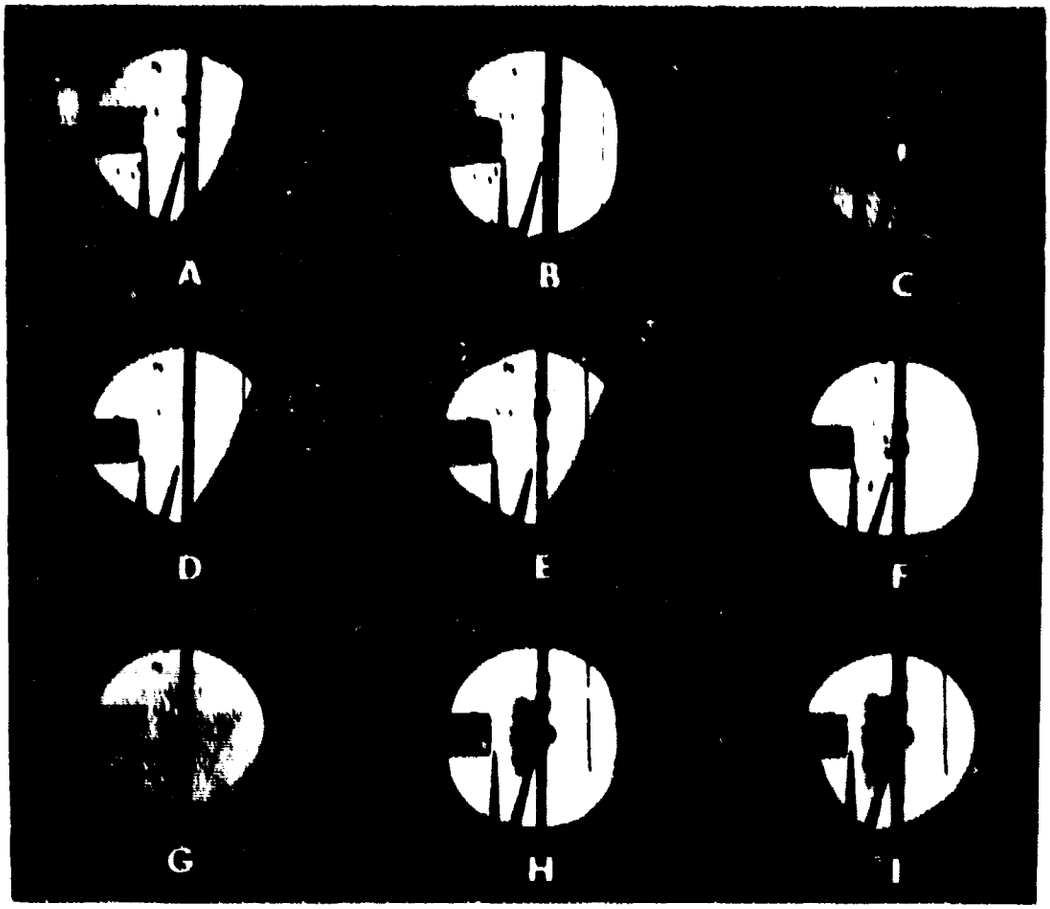

FIG. 8. Photographic Sequence. Perforation of a 0.25-inch-thick SAE 4130 steel plate by a 0.25-inch-diameter steel sphere at an initial velocity of 8,650 fps. Time of each frame in microseconds, t, relative to initial contact given by t = 1.4; 0.4; 1.5; 4.0; 5.0; 6.0; 7.8; 12.4; and 14.2 for frames (A) through (I), respectively.

until the ballistic limit is reached, then increases again while the behavior of the maximum bending strain is precisely the opposite. It was observed that the rise time of the symmetric pulse for the two highest perforation velocities corresponds almost exactly to one-half the perforation time calculated on the basis of an average projectile velocity; thus, the symmetric component may possibly mirror the perforation event to some scale when the ballistic limit is significantly exceeded. Based on the drop in speed of the projectile, an initial velocity of 5,022 fps is very near the ballistic limit for the armor plate; consequently, the peak symmetric strain occurs at a time very near that of

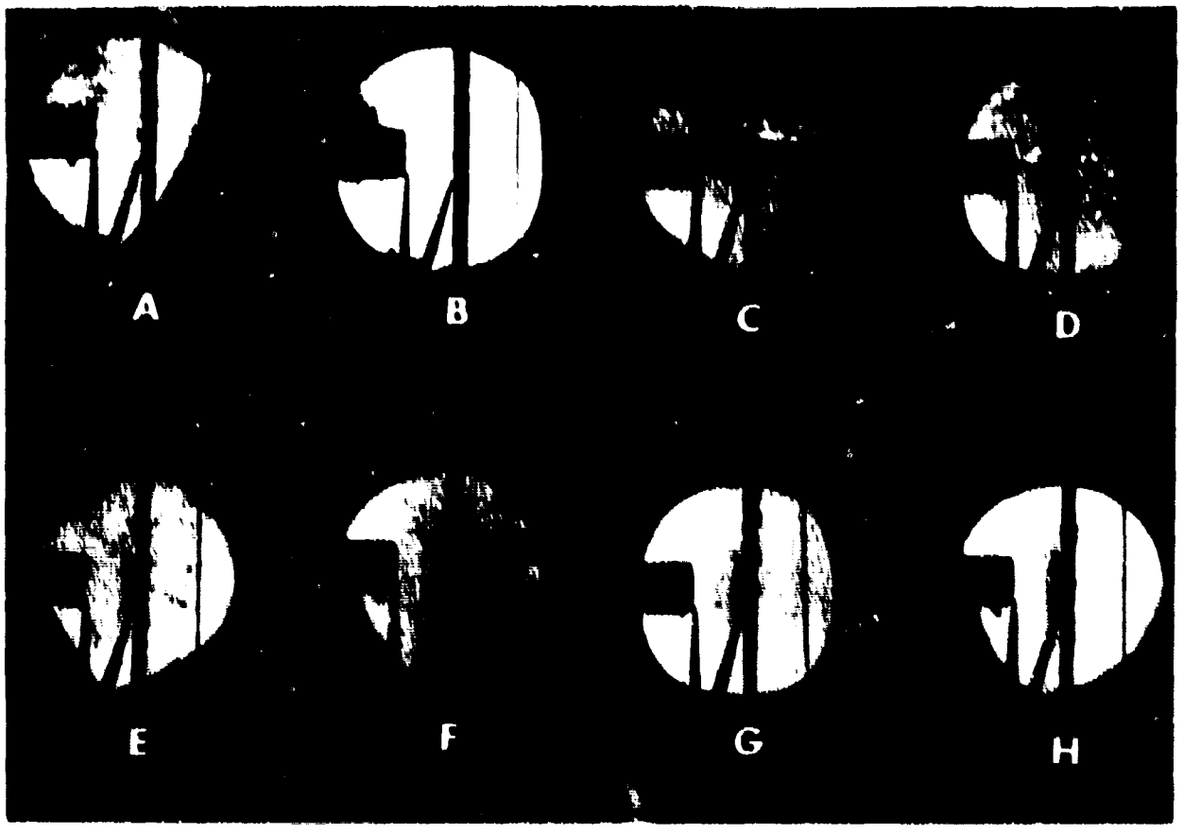

FIG. 9. Photographic Sequence. Penetration of 0.25-inch-thick SAE 4130 steel plate by a 0.25-inch-diameter steel sphere at an initial velocity of 2,900 fps. Time of each frame in microseconds, t, relative to initial contact given by t = 0; 1.7; 3.8; 4.8; 5.6; 6.5; 8.3; and 9.5 for frames (A) through (H) respectively.

the calculated perforation time based on an average projectile speed. This value has no significance in case of embedment. Conversely, the time of occurrence of the peak bending strain appears to be independent of the initial projectile velocity. If it is assumed that the initial pulse propagates with plate velocity

$$c_p = \sqrt{\frac{E}{\rho(1-\mu^2)}} = 213{,}000 \text{ in/sec} \qquad (6)$$

the peak bending strain appears to propagate with a velocity of about 60,000 in/sec out to 1.5 inches for the armor plate. Here, E is Young's

TABLE I.- Average Strain Gage and Crater Data

Target		Projectile		Average impact velocity, v_p, fps	Average velocity change, Δv, fps	Average impact velocity change, $\frac{\Delta v}{v_p}$	α	Maximum penetration depth, in.	L
Thickness, in.	Material	Diameter, in.	Material						
0.0050	2024-T4 Al	0.250	Steel ball	2360	[illegible]	[illegible]	[illegible]	[illegible]	
0.0050	do	do	do	[illegible]	[illegible]	[illegible]	[illegible]	[illegible]	
0.0050	do	do	do	do	do	do	do	[illegible]	
0.0050	2024-T4 Al	do	do	2360	[illegible]	[illegible]	0.0925[b]	0.0850	
0.0050	do	do	do	do	do	do	do	0.0850	
0.0060	do	do	do	2360	640	0.2400	0.0420[b]	0.0490	
0.0060	do	do	do	do	do	do	do	0.0450	
0.0060	do	do	2024-T4 Al foil	2290		0.2865	0.0925[b]		
0.0060	do	0.125	Steel ball	2340	570	0.1890	0.0660[b]		
0.0062	1020 Steel[d]	0.250	do	2620	1085	0.2525	0.1350[b,c]	0.0450	
0.0062	do	do	do	do	do	do	do	0.0380	
0.0062	do	do	do	4260	1024	0.1800			
0.0062	do	do	do	9060	1745	0.3485		0.0700[f]	
0.0062	do	do	do	5700	1980	0.4025	0.1195[b]	0.0490	
0.0062	do	do	do	do	do	do	do	0.0470	
0.0062	do	0.375	do	2745	490	0.1800	0.1354[b]		
0.0062	do	do	do	8420	3095	0.3990		0.0560	
0.0062	do	do	do	8960	6085	0.3990		0.0300	
0.0062	do	do	do	5,900[f]	800[f]	0.1595		0.0900	
0.0062	do	do	do	7890	1080	0.1520	0.1350[b]	0.0495	
0.125	2024-T3 Al	0.250	Steel ball	2880	590	0.2290	0.1175[b]	0.0580	
0.125	do	do	do	do	do	do	do	0.0630	
0.125	do	do	do	8850	1230	0.1385	0.1053[b]	0.0500	
0.125	do	do	do	do	do	do	do	0.0250	
0.125	do	do	do	do	do	do	do	0.0400	
0.25	2024-T4 Al	do	do	2820	1350	0.2350	0.1340[b]	0.0600	
0.25	do	do	do	do	do	do	do	0.0710	
0.25	do	do	do	8500	2250	0.1475	0.1295[b]	0.0300	
0.25	do	do	do	do	do	do	do	0.0330	
0.25	do	0.375	do	2965	735	0.1330	0.1342[b]	0.0570	
0.25	do	do	do	7915	2100	0.1590	0.1340[b]		
0.25	1020 Steel[g]	0.125	do	8700	8700[h]	0.1340	[illegible]	0.0590	

TABLE I Average Stream Gage and Crater Data.

Target		Projectile		Average initial velocity v_i, fps	Average velocity drop Av. fps	Average inner crater diam., in	Average crater depth P, in	Maximum symmetric stream, 10^{-6} oz/in	Time of occurrence msec
Thickness in	Material	Diameter in	Material						
0.050	2024-T4 Al	0.250	Steel ball	2760	230	0.250[a]	0.112[a,b]	420	8.5
0.050	do	do	do	3850	530	0.330	0.092[b]	745	3.6
0.050	do	do	do	do	do	do	do	287	3.2
0.050	2024-T4 Al	do	do	3300	360	0.347	0.078[b]	1480	1.7
0.050	do	do	do	do	do	do	do	540	4.5
0.050	do	do	do	3580	540	0.300	0.070[b]	2490	1.95
0.050	do	do	do	do	do	do	do	638	2.9
0.050	do	do	2024-T4 Al ball	3290		0.355	0.072[b]		
0.050	do	0.375	Steel ball	7840	270	0.400	0.066[b]		
0.063	1020 Steel[d]	0.250	do	3820	695	0.275	0.132[b,c]	1250	1.8
0.063	do	do	do	do	do	do	do	280	5.8
0.063	do	do	do	4310	1024	0.300	...	...	...
0.063	do	do	do	5565	1235	0.345	...	700[f]	3.4
0.063	do	do	do	3700	1980	0.402	0.115[b]	1240	5.5
0.063	do	do	do	do	do	do	do	570	1.5
0.063	do	0.375	do	2715	490	0.400	0.124[b]	...	...
0.063	do	do	do	3420	505	0.390	...	1300	5.3
0.063	do	do	do	3960	605	0.390	...	300	4.1
0.063	do	do	do	5200[f]	800[f]	0.455	...	1900	7.9
0.063	do	do	do	7850	1080	0.520	0.120[b]	1225	1.7
0.125	2024-T3 Al	0.250	Steel ball	2850	590	0.250	0.175[b]	2280	5.9
0.125	do	do	do	do.	do.	do	do	630	3
0.125	do	do	do	8550	1230	0.385	0.163[b]	1500	2.4
0.125	do	do	do	do.	do.	do.	do.	2250	3.4
0.125	do	do	do	do.	do.	do	do	400	3.0
0.25	2024-T4 Al	do	do	2820	1350	0.250	0.340[b]	1600	3.0
0.25	do	do	do	do.	do.	do	do	710	5.4
0.25	do	do	do	8500	2250	0.475	0.295[b]	2300	4.0
0.25	do	do	do	do.	do.	do	do.	1830	5.8
0.25	do	0.375	do.	2965	735	0.380	0.342[b]	1570	3.5
0.25	do	do	do	7915	2100	0.590	0.340[b]	...	...
0.25	1020 Steel[d]	0.125	do	8700	8700[h]	0.340	...	1590	3.7

TABLE 1. Average Strain Gage and Crater Data.

Projectile		Average initial velocity v_p, fps	Average velocity drop Δv, fps	Average inner crater diam., in	Average crater depth P, in	Maximum symmetric strain, 10^{-6} in/in	Time of occurrence, μsec	Maximum bending strain, 10^{-6} in/in	Time of occurrence, μsec	Strain gage position, in
ter,	Material									
	Steel ball	2760	235	0.250[d]	0.112[a,b]	420	8.5	1550	40	0.93 L
	do.	8550	530	0.330	0.092[b]	745[c]	8.6	820[c]	35	1.031 L
	do.	do.	do.	do.	do.	287	3.2	inconclusive	50	1.062 T
	do.	2800	265	0.247	0.078[b]	1480	1.7	3130	22.5	1.0 L
	do.	do.	do.	do.	do.	510	4.5	890	44	1.0 T
	do.	8580	540	0.300	0.070[b]	2190	1.95	1200	20	0.875 L
	do.	do.	do.	do.	do.	535	2.5	not evident		1.0 T
	2024 T3 Al. ball	8290	. .	0.355	0.072[b]	. . .	. . .			. .
	Steel ball	7840	270	0.400	0.066[b]	. . .	. . .			. .
	do.	2820	695	0.275	0.132[b,c]	1250	1.8	2600	24.7	1.0 L
	do.	do.	do.	do.	do.	280	5.8	720	51	1.0 T
	do.	4310	1024	0.300	. . .	. . .	. . .	.	.	.
	do.	5565	1235	0.345	. . .	700[f]	3.4	2700	26[f]	1.0 L
	do.	8700	1980	0.402	0.115[b]	1240	5.5	1500[f]	20	1.0 L
	do.	do.	do.	do.	do.	570	1.5	not evident		1.0 T
	do.	2745	490	0.400	0.124[b]	. . .	. . .	. . .		
	do.	3420	505	0.390	. . .	1300	5.3	1690	3.0	1.5 L
	do.	3960	605	0.390	. . .	300	4.1	280	20	1.5 T
	do.	5200[f]	800[f]	0.455	. . .	1900	7.9	1220	26.5	1.5 L
	do.	7850	1080	0.520	0.120[b]	1225	1.7	not evident		1.562 L
	Steel ball	2850	590	0.250	0.175[b]	2280	5.9	3300	19	1.0 L
	do.	do.	do.	do.	do.	630	3	inconclusive	.	1.0 T
	do.	8550	1230	0.385	0.163[b]	1500	2.4	3200	16	1.0 L
	do.	do.	do.	do.	do.	2250	3.4	2100	20	1.375 L
	do.	do.	do.	do.	do.	400	3.0	inconclusive		1.562 T
	do.	2820	1350	0.250	0.340[b]	1600	3.0	3660	13.7	1.0 T
	do.	do.	do.	do.	do.	710	5.4	1600	21.5	1.0 L
	do.	8500	2250	0.475	0.295[b]	2300	4.0	1000	10	1.5 L
	do.	do.	do.	do.	do.	1830	5.8	900	27	1.5 T
	do.	2965	735	0.380	0.342[b]	1570	3.5	3880	21.2	1.5 L
	do.	7915	2100	0.590	0.340[b]	. . .	. . .	. . .		.
	do.	8700	8700[h]	0.340	. . .	1590	3.7	1500	19.2	1.45 L

TABLE 1. (Contd.)

Target		Projectile		Average initial velocity	Average velocity drop Δv,	Average inner crater	Average crater depth	Maximum symmetric strain,	Time of occurrence μsec	M
Thickness, in	Material	Diameter, in	Material							
0.25	Steel[f]	0.250	Steel ball	2800	2800[h]	0.250	0.244[i]	...	...	
0.25	do.	do.	do.	8600	5300	0.540	0.434[h]	...	...	
0.25	1020 Steel[g]	do.	do.	2840	2840[h]	0.250	0.226	930	2.3	
0.25	do.	do.	do.	do.	do.	do.	do.	250	7.1	
0.25	do.	do.	do.	4310	3900	0.320	...	360	3.8	
0.25	do.	do.	do.	do.	do.	do.	...	400	3.4	not
0.25	do.	do.	do.	do.	do.	do.	...	450	3.0	
0.25	do.	do.	do.	do.	do.	do.	...	530	3.0	
0.25	do.	do.	do.	do.	do.	do.	...	1290	1.7	
0.25	do.	do.	do.	4330	3754	0.347	...	1400	2.6	
0.25	do.	do.	do.	4835	4116	0.410	...	1650	5.6	
0.25	do.	do.	do.	6940	4575	0.475	...	2380	not well defined	
0.25	do.	do.	do.	8970	5660	0.520	...	1700	2.7	
0.25	do.	do.	do.	do.	do.	do.	...	840	6.4	
0.25	4130 Steel	do.	do.	2900	2900[h]	0.310	0.108[i]	1010	3.1	
0.25	do.	do.	do.	do.	do.	do.	do.	250	4	
0.25	do.	do.	do.	3660	3660[h]	0.300	...	not evident	...	
0.25	do.	do.	do.	4520	4520[h]	0.250	...	2520	3.0	
0.25	do.	do.	do.	5022	4334	0.295	...	1990	6.4	
0.25	do.	do.	do.	6960	4840	0.405	...	2640	2.6	
0.25	do.	do.	do.	8150	5340	0.47	...	2000	2	
0.25	do.	do.	do.	do.	do.	do.	...	3160	3.2	
0.25	do.	do.	do.	8670	5700	0.480	0.368[h]	3040	2.6	
0.25	do.	do.	do.	do.	do.	do.	do.	820	5.0	

[a] Dished additionally by about 1 plate thickness
[b] Impact lip to exit lip
[c] Single gage only
[d] Small grained, well annealed
[e] Dishing by 1/3 plate thickness
[f] Estimated
[g] Large grained, poorly annealed
[h] No perforations
[i] Impact lip to crater depth
L Longitudinal
T Tangential

TABLE 1. (Contd.)

le Material	Average initial velocity	Average velocity drop Δv,	Average inner crater	Average crater depth	Maximum symmetric strain,	Time of occurrence μsec	Maximum bending strain,	Time of occurrence μsec	Strain gage position, in
l ball	2800	2800[h]	0.250	0.244[i]	...	...	...	...	...
	8600	5300	0.540	0.434[h]	...	...	...	...	...
	2840	2840[h]	0.250	0.226	930	2.3	2270	24.5	1.5 L
	do.	do.	do.	do.	250	7.1	670	34.5	1.5 T
	4310	3900	0.320	...	360	3.8	800	61	7.5 L
	do.	do.	do.	...	400	3.4	not measurable	...	9.0 L
	do.	do.	do.	...	450	3.0	1060	31	3.0 L
	do.	do.	do.	...	530	3.0	710	36.5	4.5 L
	do.	do.	do.	...	1290	1.7	2850	12.2	1.6 L
	4330	3754	0.347	...	1400	2.6	2950	24.9	1.5 L
	4835	4116	0.410	...	1650	5.6	...	...	1.5 L
	6940	4575	0.475	...	2380	not well defined	2040	26	1.5 L
	8970	5660	0.520	...	1700	2.7	2100	23.5	1.5 L
	do.	do.	do.	...	840	6.4	880	36.6	1.5 T
	2900	2900[h]	0.310	0.108[i]	1010	3.1	2600	17.3	1.687 L
	do.	do.	do.	do.	250	4	600	35	1.58 T
	3600	3660[h]	0.300	...	not evident	...	2640	20	1.6 L
	4520	4520[h]	0.250	...	2520	3.0	3000	17.2	1.45 L
	5022	4334	0.295	...	1990	6.4	3100	19.8	1.42 L
	6960	4840	0.405	...	2640	2.6	1350	19.3	1.5 L
	8150	5340	0.47	...	2000	2	1550	18	1.5 L
	do.	do.	do.	...	3160	3.2	1200	24	1.5 T
	8670	5700	0.480	0.368[h]	3040	2.6	855	21.7	1.5 L
	do.	do.	do.	do.	820	5.0	470	26	1.5 T

kness

modulus, 29.6 x 10^6 lb/in^2, ρ the mass density, 0.0007358 lb-sec^2/in^4, and μ is Poisson's ratio, 0.29 for steel.

The studies with mild steel perforated at an initial velocity of 4,310 fps indicate an initial drastic reduction of the symmetric strain with distance from the impact point that flattens out rapidly with increased separation from the contact position. A similar trend is observed for the amplitude of the bending strain, but while the rise of the symmetric component is nearly the same at all stations, that for the bending strain becomes less steep at more distant locations. Based on the same plate velocity as given above, the peak bending strain appears to travel here with a nearly constant velocity of about 80,000 in/sec out to at least 7.5 inches from the impact point. At similar positions the amplitude of the symmetric strain varied directly as, and the amplitude of the antisymmetric strain varied inversely as the initial velocity for almost all targets, the latter changes being more pronounced.

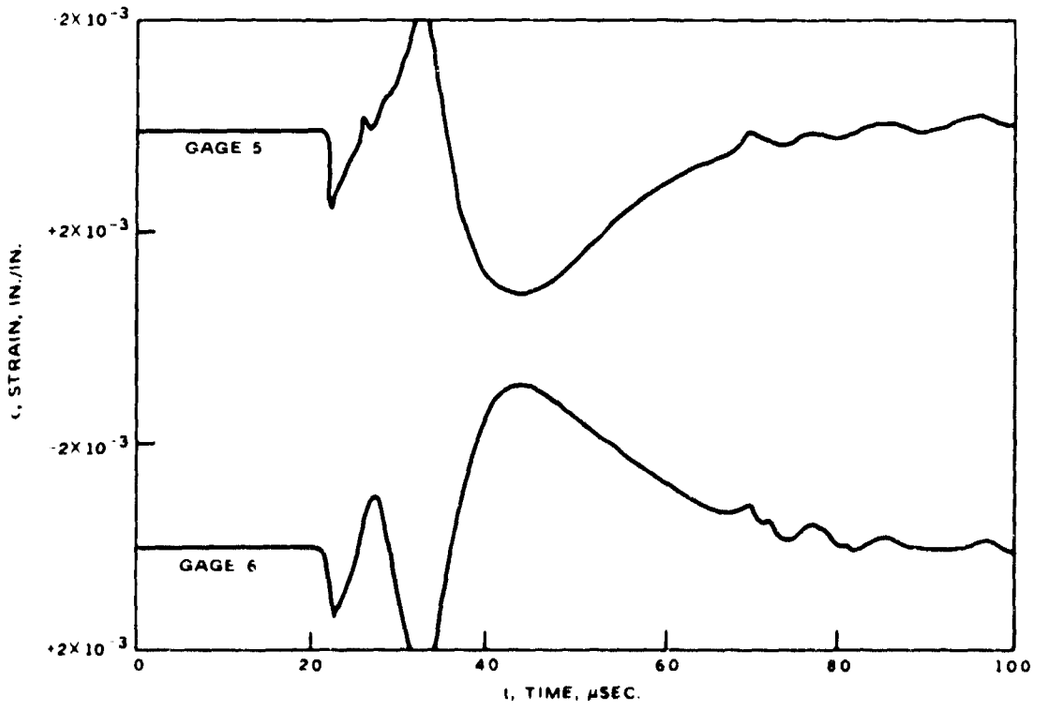

FIG. 10. Strain Gage Record. Longitudinal strain histories 1 inch from the impact point in a 0.050-inch-thick 2024-T3 aluminum plate perforated by a 0.25-inch steel sphere with an initial velocity of 2,795 fps.

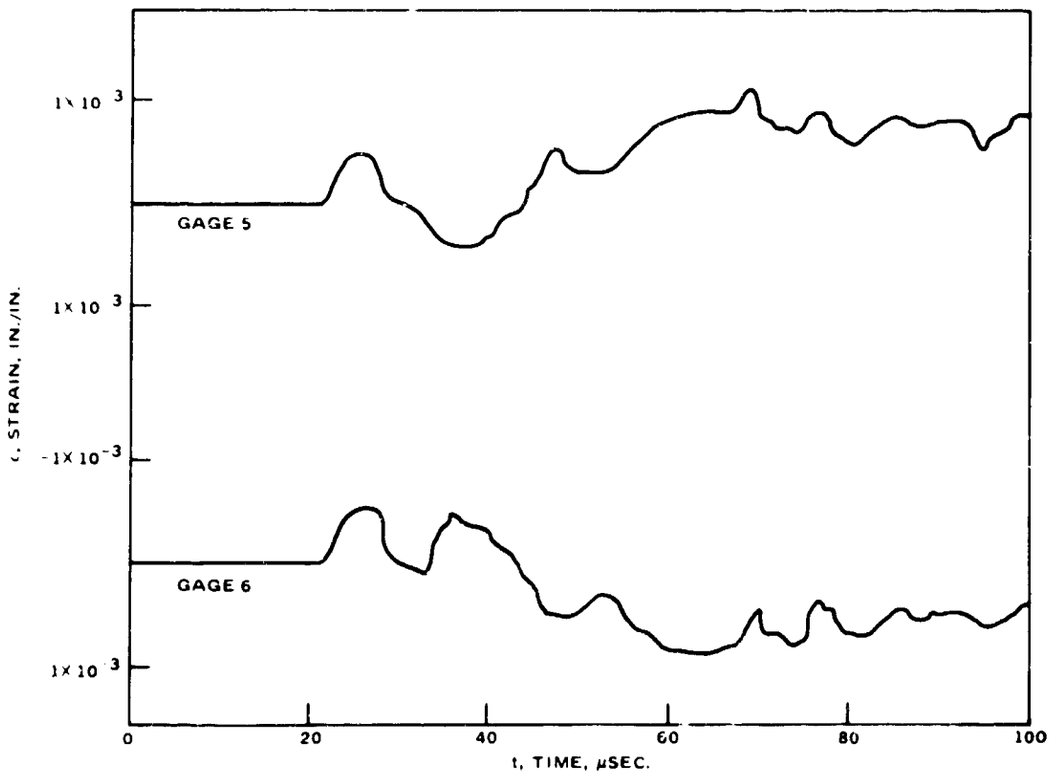

FIG. 11. Strain Gage Record. Transverse strain histories 1 inch from the impact point in a 0.050-inch-thick 2024-T3 aluminum plate perforated by a 0.25-inch-diameter steel sphere with an initial velocity of 2,685 fps.

By and large, little difference in these parameters was observed when the diameter of the projectile was increased by 50 percent. Nearly identical magnitudes of symmetric and bending strains were obtained at initial velocities of about 8,800 fps in 0.25-inch-thick mild steel targets by both 0.125-inch and 0.25-inch-diameter projectiles even though the smaller projectile failed to perforate. This is probably a coincidence.

The displacement-time curves of the projectile for a selected set of impact conditions utilized in the determination of the force histories are shown in Fig. 16 through 22. The horizontal dashed lines spanning these curves and forming their envelope have a length equal to the target thickness and hence represent the maximum degree of uncertainty in the location of the projectile positions. Since both the front of the bulge and the rear of the sphere are simultaneously visible in a number of photographs, the dual data so plotted serves to reduce this region of

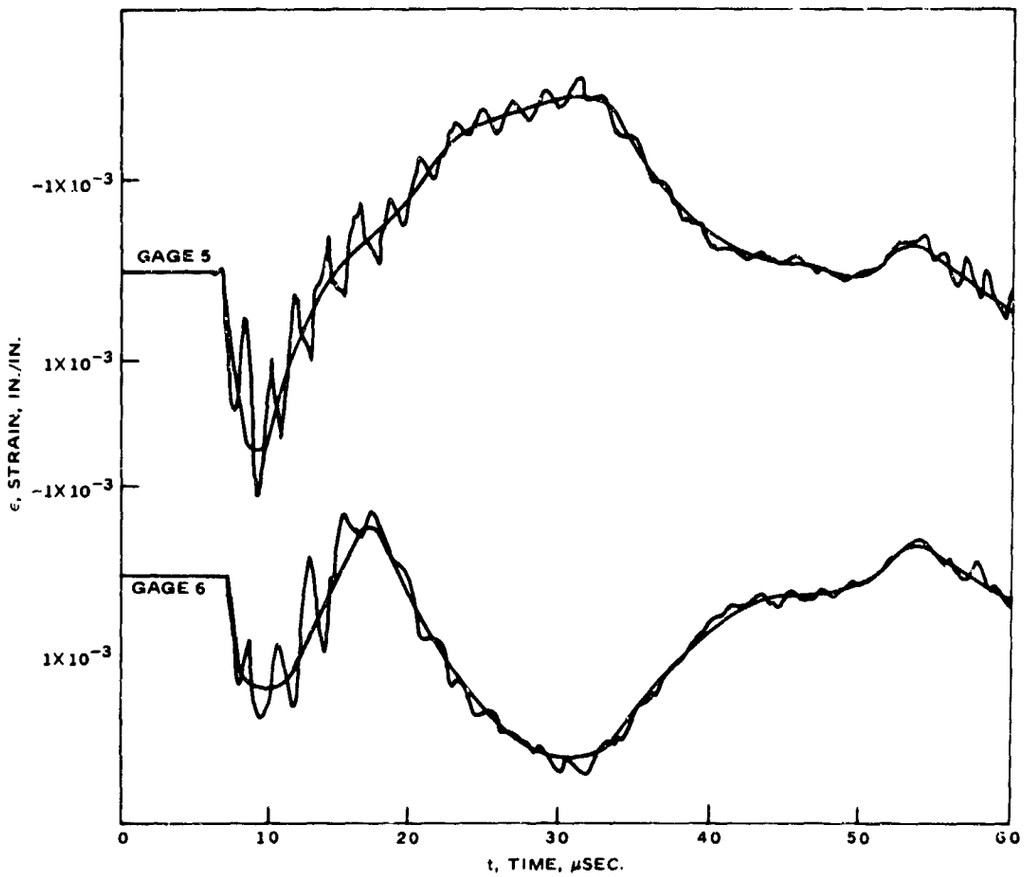

FIG. 12. Strain Gage Record. Longitudinal strain histories 1.5625 inches from the impact point in a 0.25-inch-thick SAE 1020 large-grained steel plate perforated by a 0.25-inch-diameter steel sphere with an initial velocity of 8,900 fps.

uncertainty. Figure 23 shows the computer output of the displacement, velocity and acceleration history for the data presented in Fig. 16, derived from Eq. (2) and (4). The contact force in pounds is obtained from the acceleration curve upon multiplication by 6.06×10^{-6} lb-sec^2/in or 2.06×10^{-5} lb-sec^2/in for the 0.25-inch or 0.375-inch-diameter steel spheres, respectively. Figures 24 and 25 portray the force histories corresponding to Fig. 16 through 21. Figure 26 shows the corresponding results for the nonperforation case of Fig. 22, derived from Eq. (1) and (3). Table 2 summarizes the pertinent experimental and computer results for all primary runs, and includes the constants for the empirical equations evaluated by means of a least square fit (Ref. 1) for tests with camera observation. It should be emphasized here that the coefficient D is completely arbitrary, representing solely a translation along the

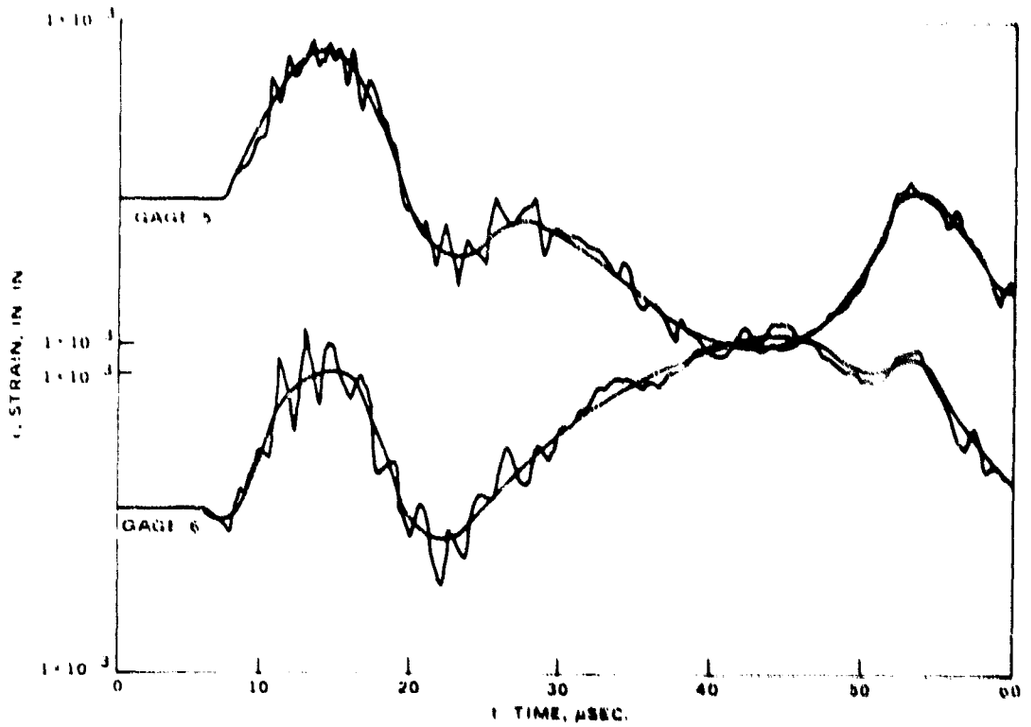

FIG. 13. Strain Gage Record. Transverse strain histories 1.4375 inches from impact point in a 0.25-inch-thick SAE 1020 large-grained steel plate perforated by a 0.25-inch-diameter steel sphere with an initial velocity of 9,040 fps.

displacement axis. Table 2 also includes the computed value of the final velocity as given by Eq. A-4 based on measured or estimated plug dimensions, b. Values of the ultimate tensile and shear strength, σ_u and σ_s, respectively, as well as other mechanical properties, are given in Table 3.

Photographs of the craters, both face-on and in section, are shown in Fig. 27 and 28. Figure 29 portrays sections of the mild steel and armor plate targets in which a 0.25-inch-diameter steel sphere striking at a velocity of 2,900 was embedded. Both of these targets show significant petalling, flattening of the projectile, and a bulge on the distal side, but the armor plate annihilates the shape of the striker and also exhibits a smaller deformation on the opposite face than in the case of the mild steel, indicative of its greater resistance to perforation. Figure 30 photographically depicts the perforation event 25 microseconds after contact of a 0.25-inch-diameter steel bullet striking a 0.25-inch-thick mild steel plate just above the ballistic limit at a velocity of 4,310 fps. The geometry of the projectile may still be recognized,

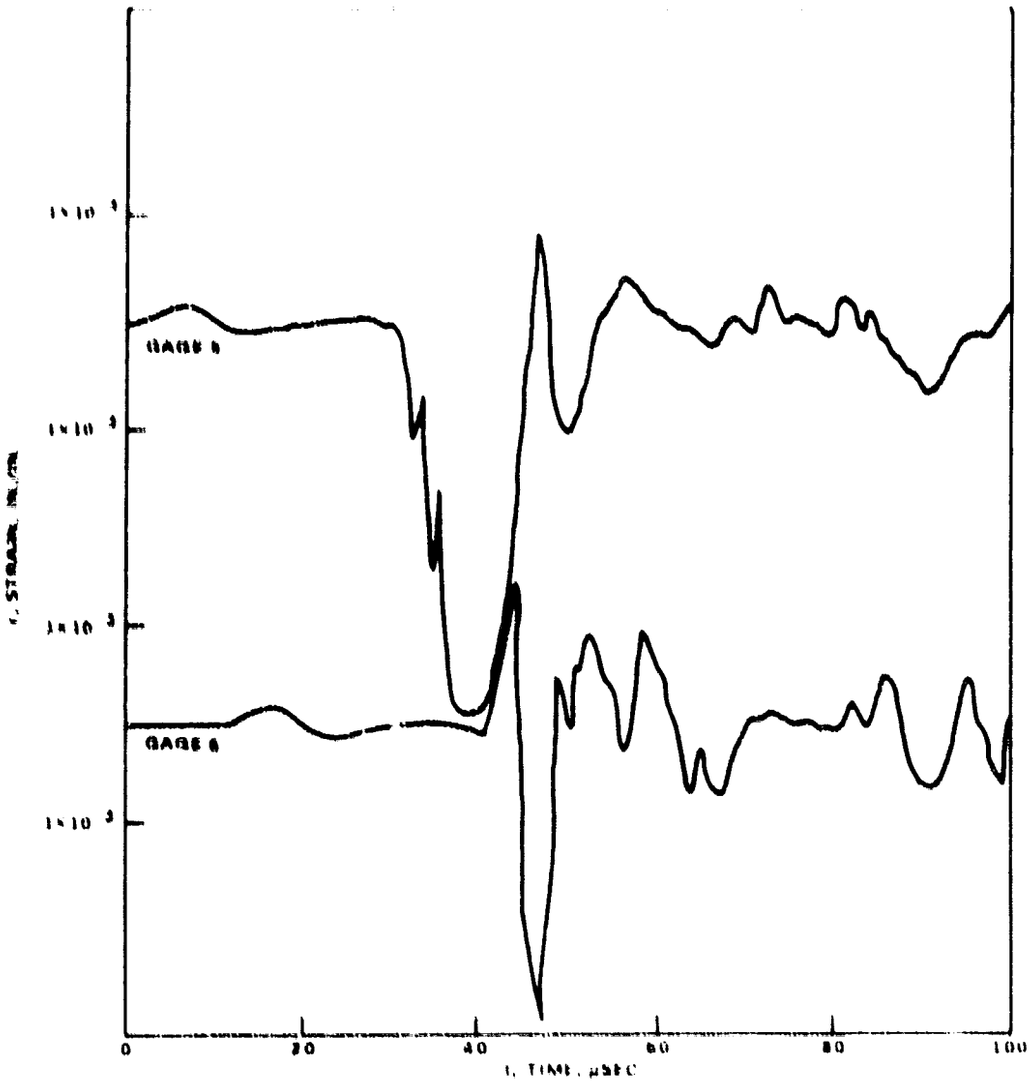

FIG. 14. Strain Gage Record. Longitudinal strain histories 1.6250 inches from the impact point in a 0.25-inch-thick SAE 4130 steel plate penetrated by a 0.25-inch-diameter steel sphere with an initial velocity of 2,910 fps.

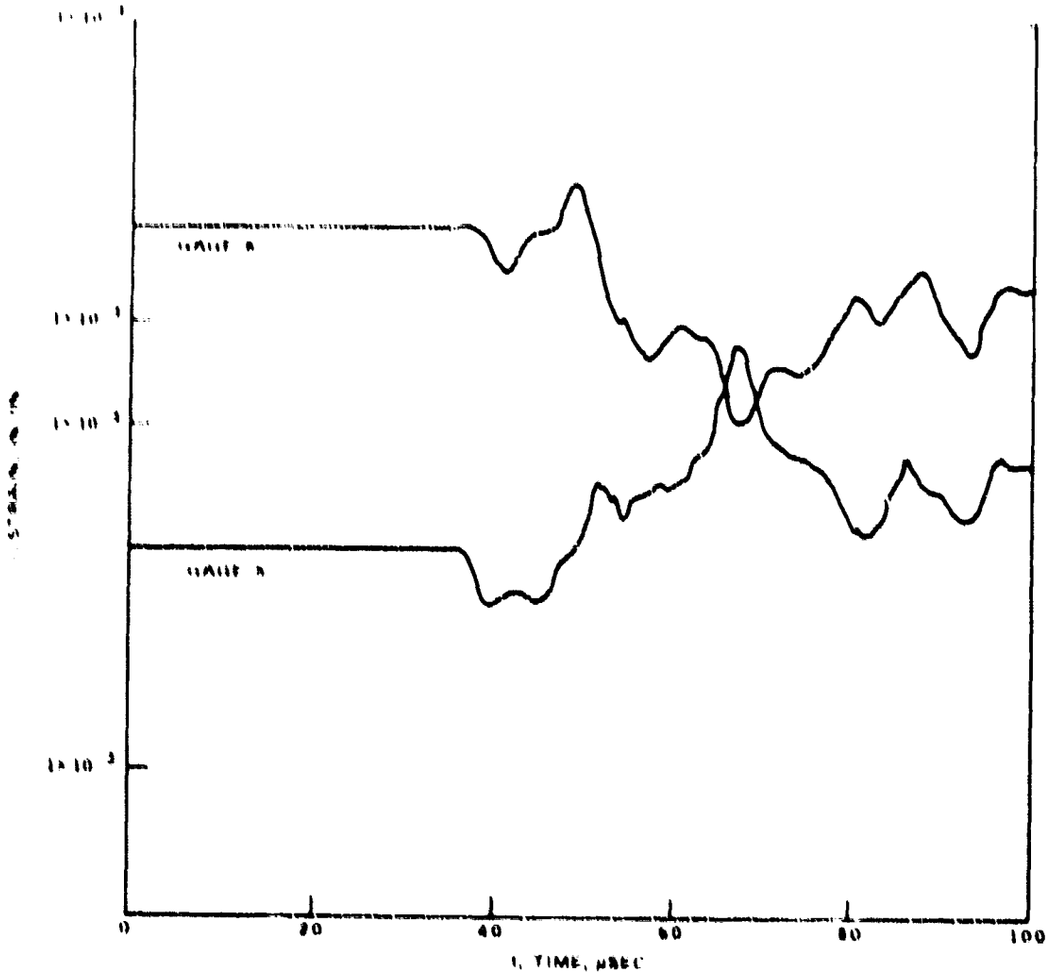

FIG. 15. Strain Gage Record. Transverse strain histories 1.6250 inches from impact point in a 0.25-inch-thick SAE 4130 steel plate penetrated by a 0.25-inch-diameter steel sphere with an initial velocity of 2,515 fps.

although significant fragmentation of both bullet and target have ensued, and an elliptic envelope representing the shock wave emanating from the distal side of the target, partly filled with debris, is clearly evident. Figure 31 presents another late view of the perforation process in a thin steel target performed at high velocity, where the striker is substantially pulverized.

Figure 32 shows a plot of the projectile velocity drop, Δv, as a function of initial velocity v_i. A general drop in Δv is observed with decreasing impact velocity except in the vicinity of the ballistic limit $\Delta v = v_i$, where an increase in the former is noted. The data from the ballistic limit tests are incorporated in this diagram.

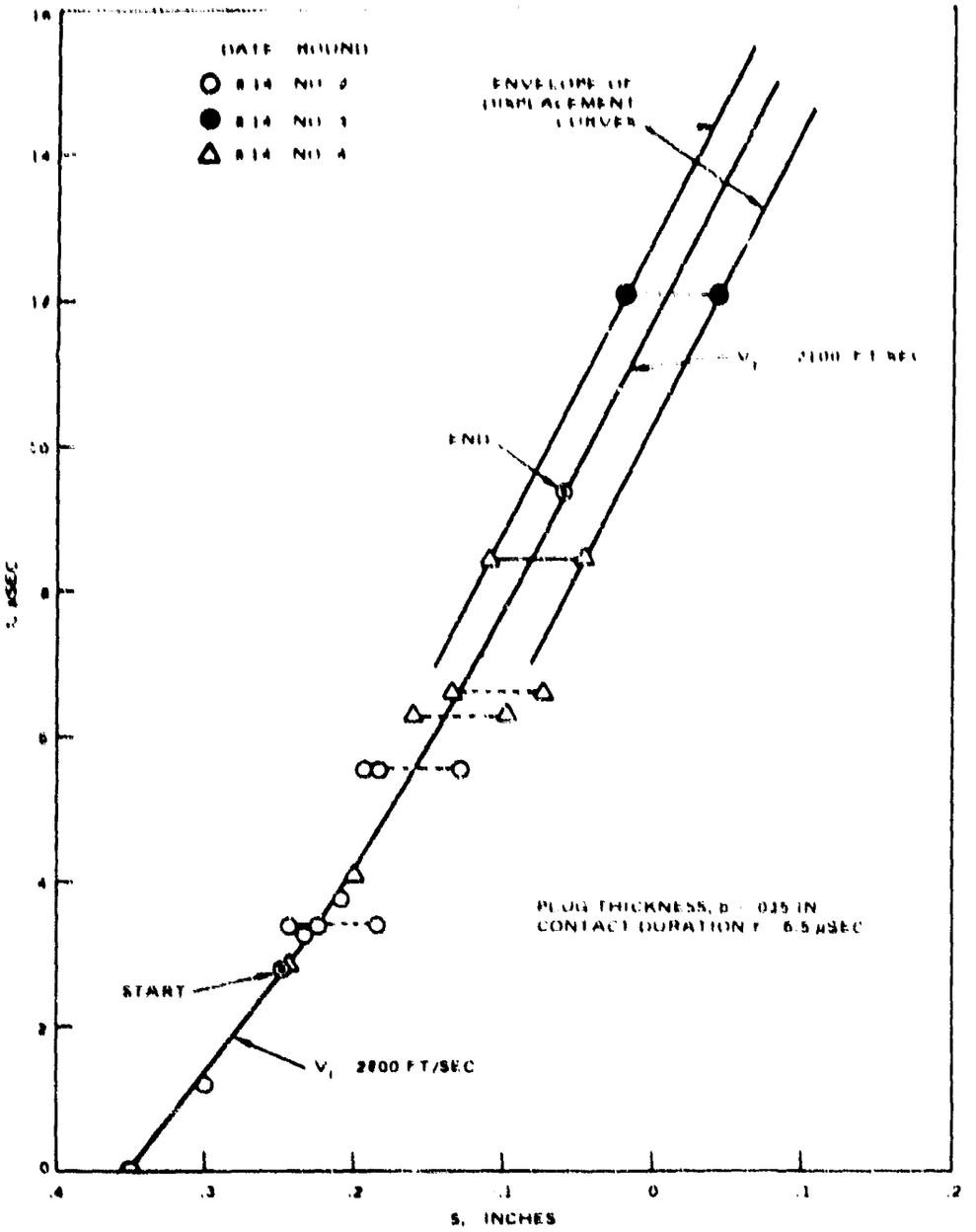

FIG. 16. Displacement-Time Curve. A 0.25-inch-diameter steel sphere with an initial velocity of 2,800 fps perforating a 0.062-inch-thick SAE 1020 steel plate.

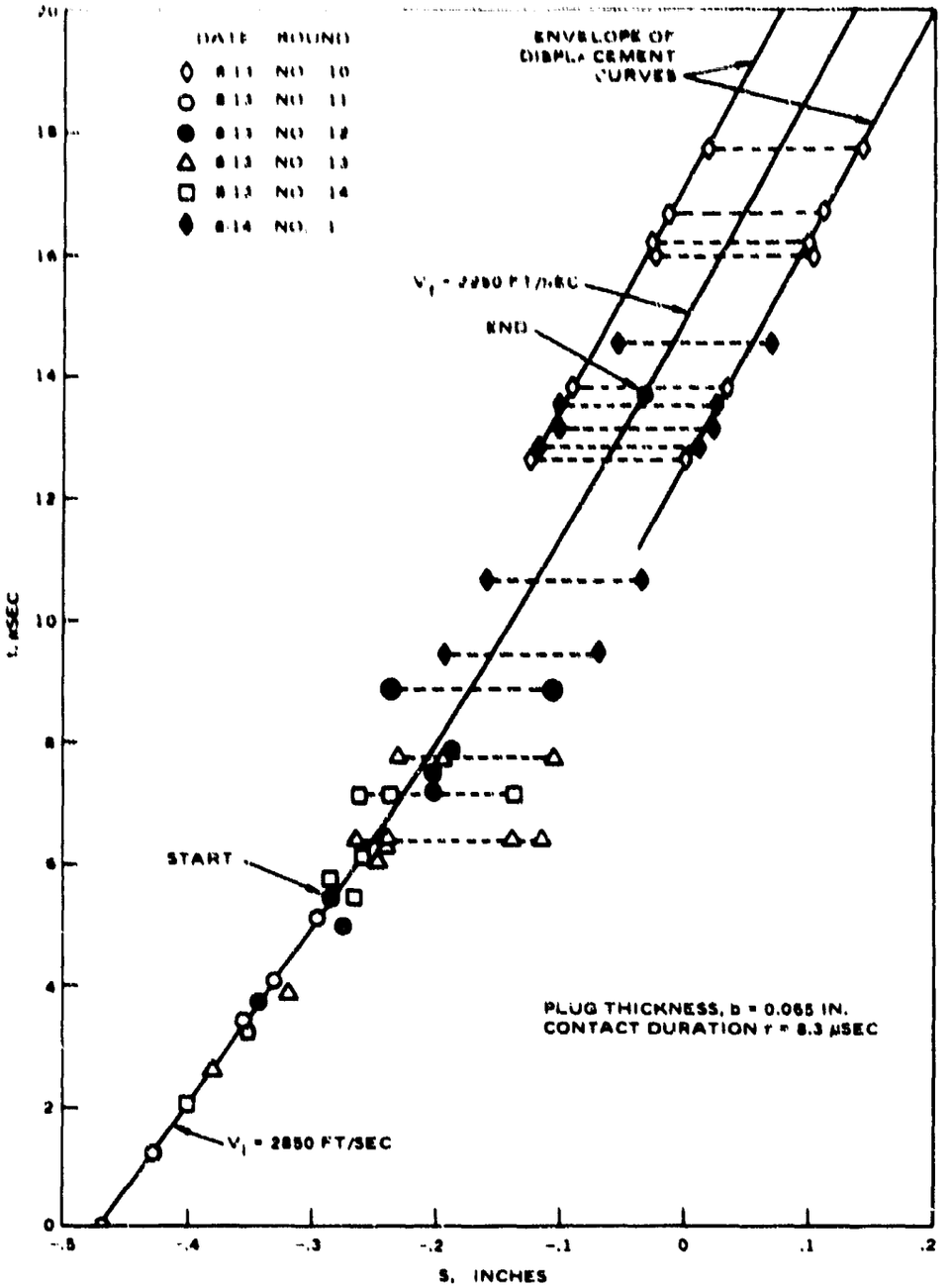

FIG. 17. Displacement-Time Curve. A 0.25-inch-diameter steel sphere with an initial velocity of 2,850 fps perforating a 0.125-inch-thick 2024-T3 aluminum plate.

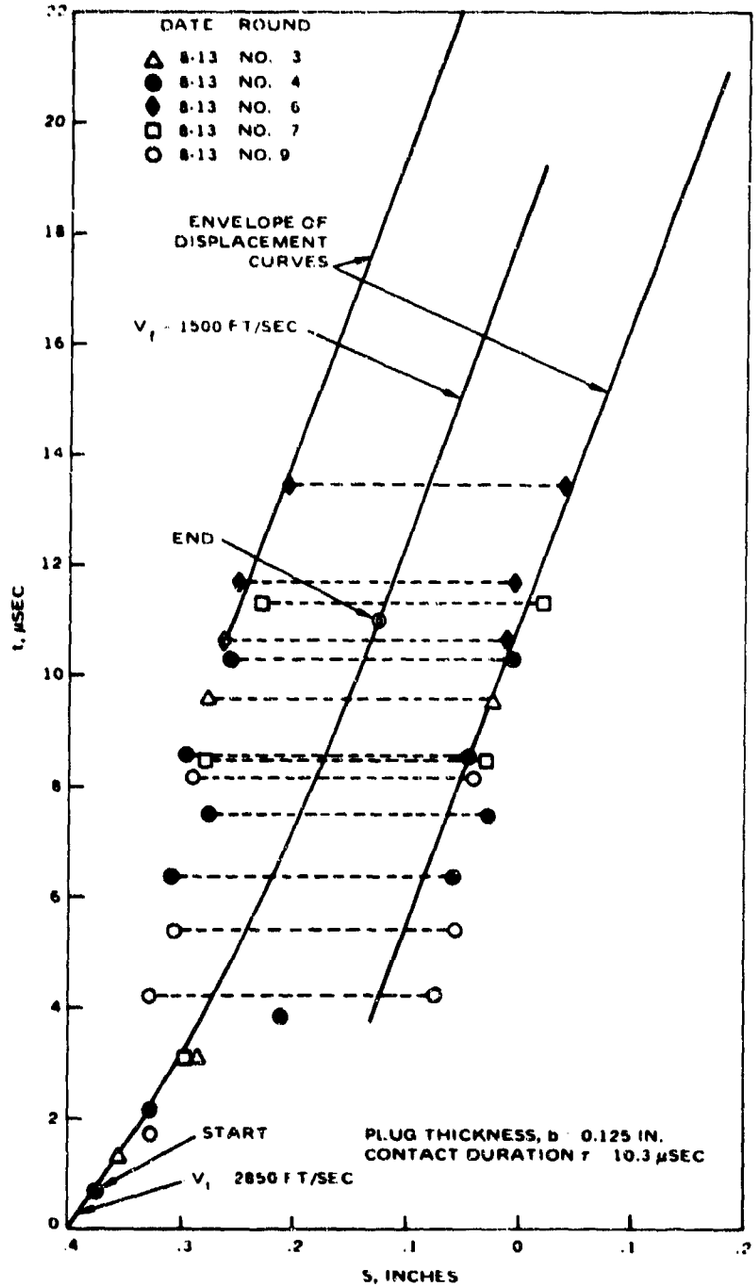

FIG. 18. Displacement-Time Curve. A 0.25-inch-diameter steel sphere with an initial velocity of 2,850 fps perforating a 0.25-inch-thick 2024-T-4 aluminum plate.

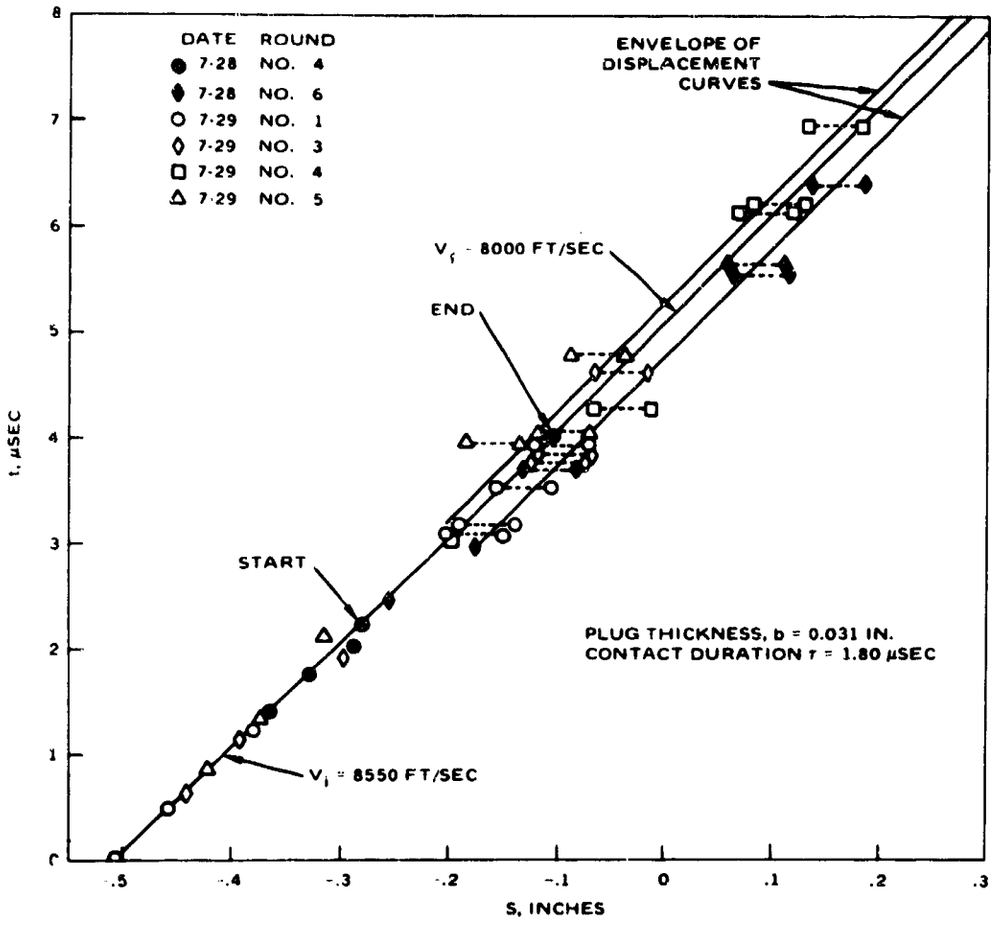

FIG. 19. Displacement-Time Curve. A 0.25-inch-diameter steel sphere with an initial velocity of 8,550 fps perforating a 0.05-inch-thick 2024-0 aluminum plate.

Figure 33 shows the quasistatic tensile stress-strain curves for the various targets employed, reproduced either from available data (Ref. 35) or plotted from current tests. The data for 2024-T3 aluminum is presumed to be the same as that in the T4 condition.

DISCUSSION

The present investigation of projectile impact on metallic plates covers a range of initial velocities of approximately 3 to 1. The lowest impact speed of about 2,800 fps is well above the ballistic limit for all aluminum targets and for the thin steel targets employed, but constitutes only 50 to 60 percent of the ballistic limit for the 0.25-inch-thick steel

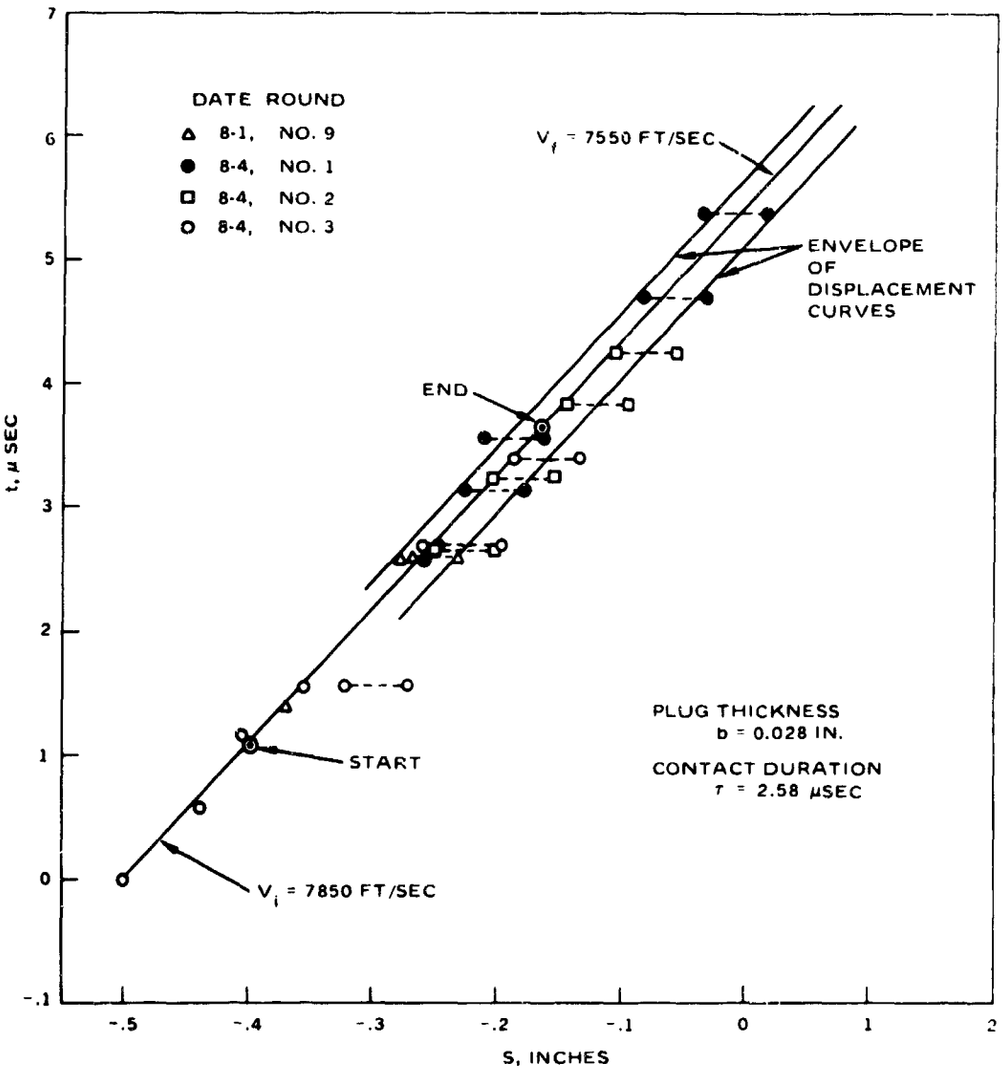

FIG. 20. Displacement-Time Curve. A 0.375-inch-diameter steel sphere with an initial velocity of 7,850 fps perforating a 0.05-inch-thick 2024-T3 aluminum plate.

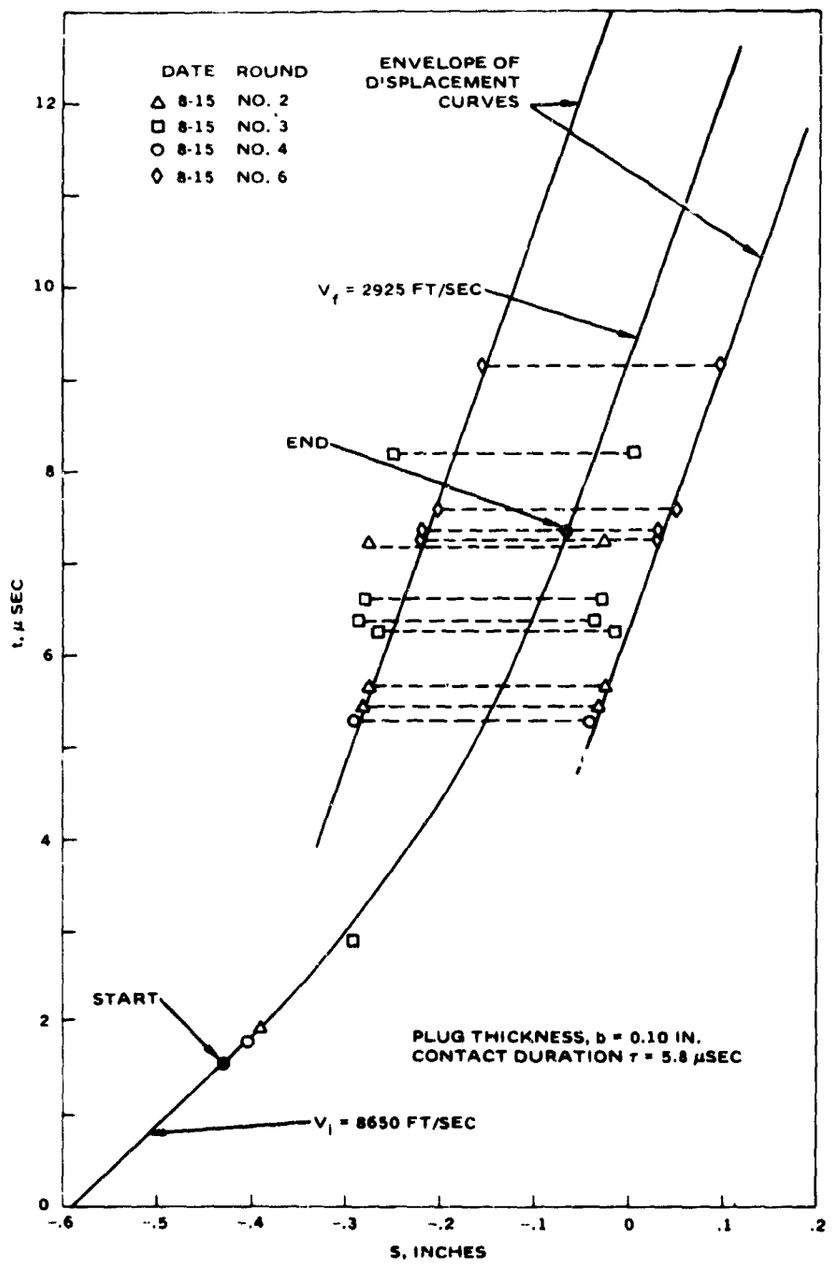

FIG. 21. Displacement-Time Curve. A 0.25-inch-diameter steel sphere with an initial velocity of 8,650 fps perforating a 0.25-inch-thick SAE 4130 steel plate.

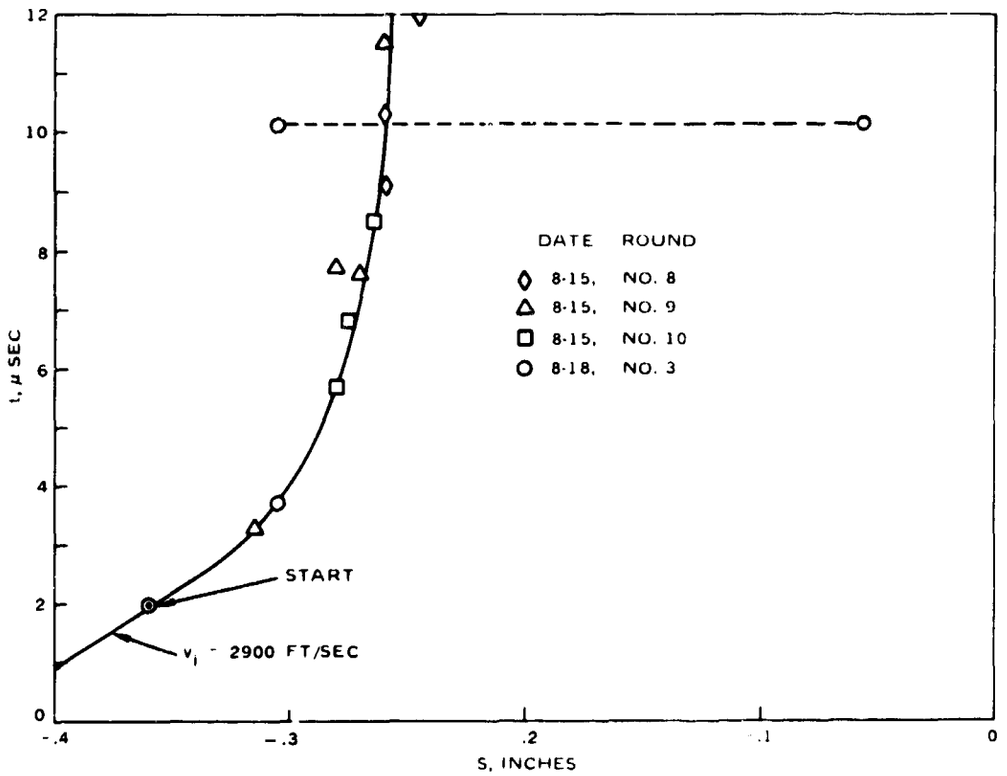

FIG. 22. Displacement-Time Curve. A 0.25-inch-diameter steel sphere with an initial velocity of 2,900 fps penetrating a 0.25-inch-thick SAE 4130 steel plate.

plates. In consequence, perforation is always present in the first case, but ensues only with increasing initial projectile speed in the second instance, with penetration occurring at the lower velocities. The program was initially designed to extend the previous investigation of target penetration and perforation of soft aluminum sheets by 0.5-inch-diameter spherical projectiles (Ref. 1, 5) to higher velocity regimes but this objective required the use of sabots thus necessitating a reduction in the size of the projectile to permit the use of available equipment. The tests were also extended to other target materials and thicknesses. These modifications make it difficult to attain direct comparisons with the results of earlier experiments. Correlations of the data with that obtained in other investigations (Ref. 2), is even more tenuous since the impact conditions and objectives are completely different.

As in similar investigations, these tests relied upon repeatability of the event for many portions of the data reduction procedure. Sandwiching of the camera results is the most prominent example of this

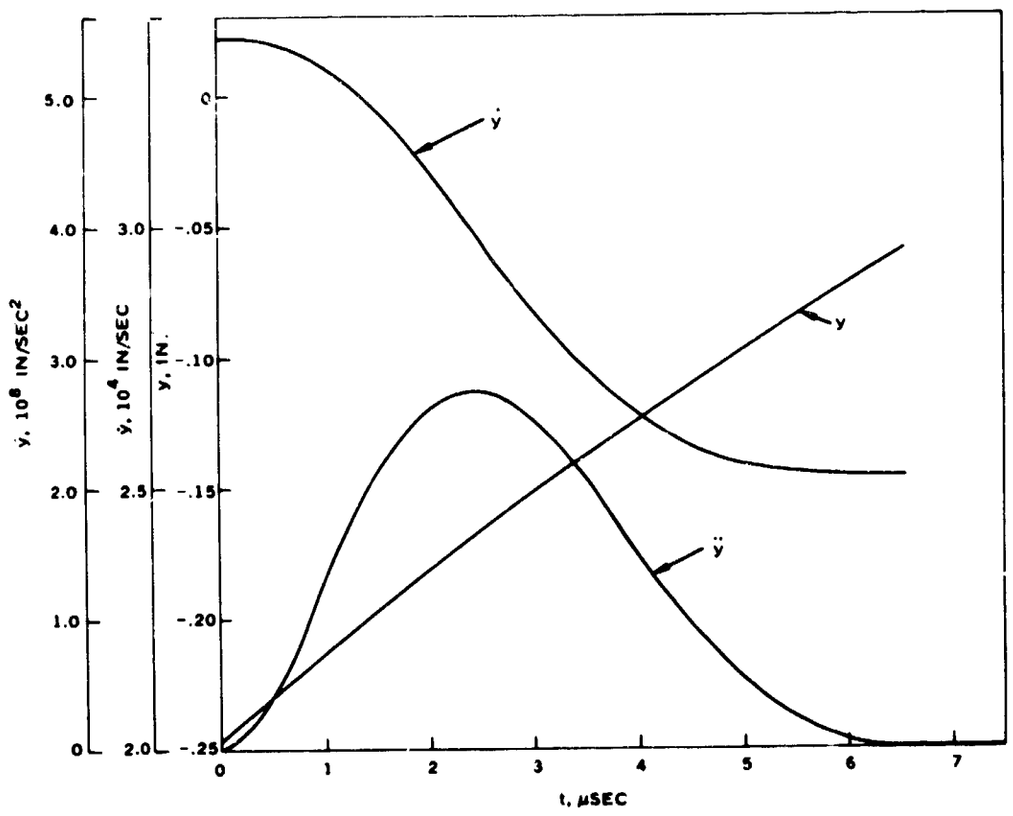

FIG. 23. Computed Displacement, Velocity, and Acceleration History. Perforation of a 0.062-inch SAE 1020 steel plate by a 0.25-inch-diameter steel sphere travelling with an initial velocity of 2,800 fps.

process, accomplished with an accuracy of about ±0.2 μsec. The strain gage information was obtained from runs without camera coverage, as the condenser discharge produced spurious effects on the strain records completely obliterating the actual pulse.

As noted in Ref. 1, damage to the thin targets as measured by the amount of permanent deformation in the impact region increased here also up to the ballistic limit and then sharply diminished with greater impact velocity. The data did not substantiate such a discontinuity for the 0.25-inch-thick steel targets. The soft aluminum plates, Type 0, exhibited more dishing at the lower impact velocities, of the order of 0.01 inch, than was observed in the other thin targets. This deformation compares to the severe dishing and local plastic flow involving central deflections of about 0.5 inch for soft aluminum plates struck by 0.5-inch-diameter steel spheres at a velocity of 497 fps, just above the ballistic limit (Ref. 1). The larger projectile would be expected to produce much larger bending effects. There, the cap sheared from the target assumed

the shape of a spherical segment conforming to the surface of the perforating projectile, with the diameter approaching that of the bullet as the highest velocity (about 1,000 fps) was approached. This process constituted a reduction in the degree of plastic bending of the plate and hence in the depth of the cylindrical crater as the impact velocity was increased. This differs from the purely geometric fracture pattern found in this type of plate upon low-speed perforation by a conical-nosed projectile where this phenomenon is initiated when the plate becomes tangent to the conical surface at the contact point as the result of bending (Ref. 5).

In the present tests, caps were also obtained for all thin targets at the lowest impact velocities, but the sphericity of this part decreased with the plate ductility from soft aluminum to mild steel to 2024-T3 aluminum. No evidence of fragmentation could be found in the first two materials and very little in the last; however, both the plug and the target exhibited shearing effects at this velocity in the 0.125- and 0.25-inch-thick aluminum plates. The projectile was found to flatten and fracture extensively in the penetration tests involving 0.25-inch-thick mild steel and armor plate.

With increased impact velocity, the perforation process in the thin targets was converted into a punching operation, particularly in the case of the soft aluminum. At initial projectile speeds of about 5,000 fps, just in excess of the ballistic limit for the SAE 4130 steel target, the plugs formed from the 0.25-inch-thick plates were reasonably hemispherical in the case of mild steel, but less so in the case of 2024-T4 aluminum and armor plate. Additional ring-shaped fragments were expelled

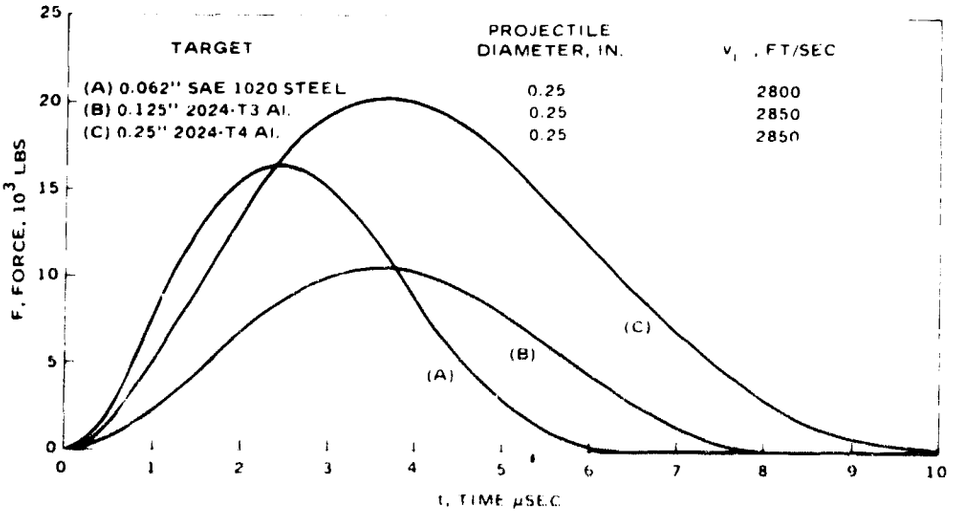

FIG. 24. Force-Time Curves for the Data Corresponding to Fig. 16 Through 18.

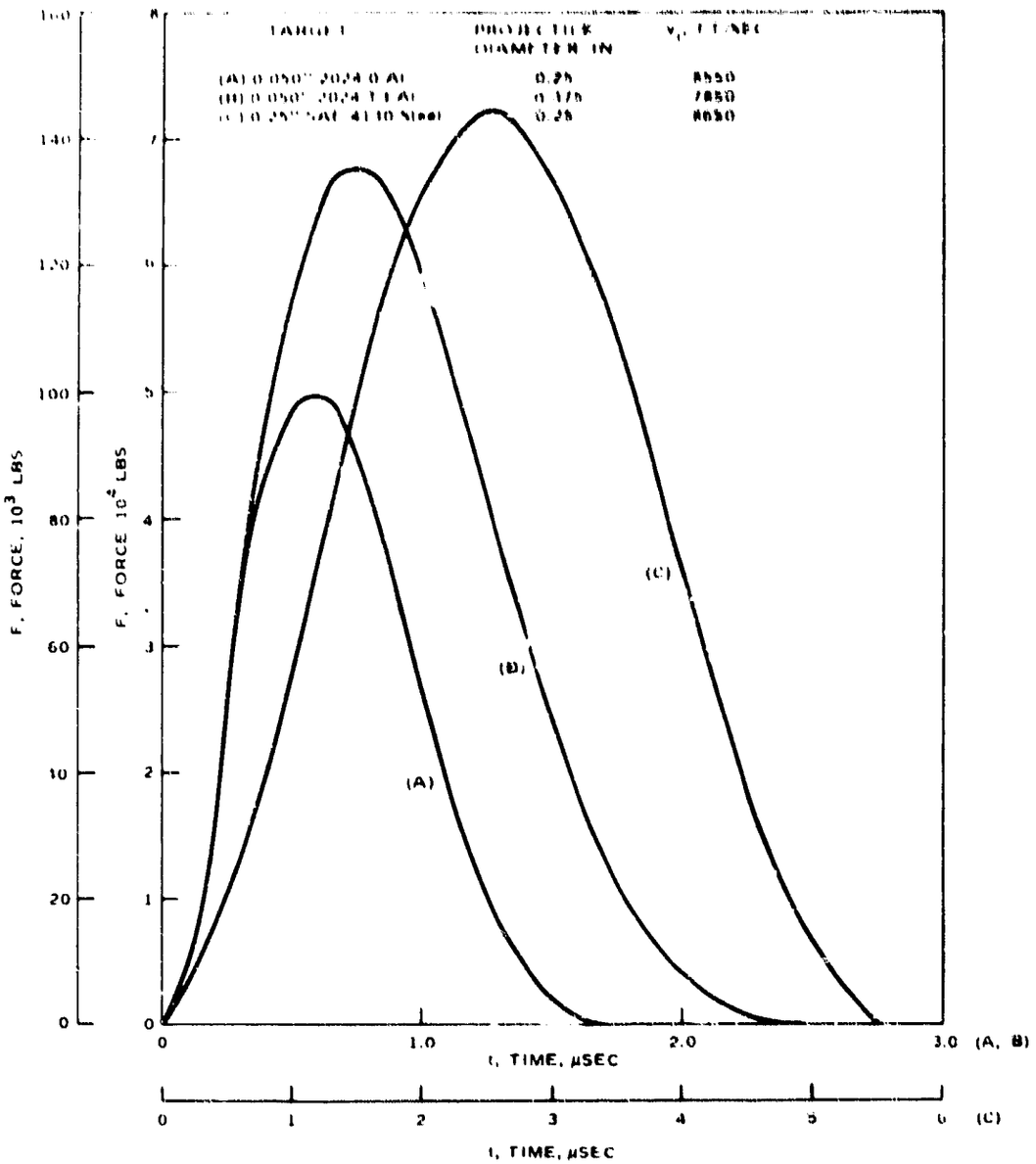

FIG. 25. Force-Time Curves for the Data Corresponding to Fig. 19 Through 21.

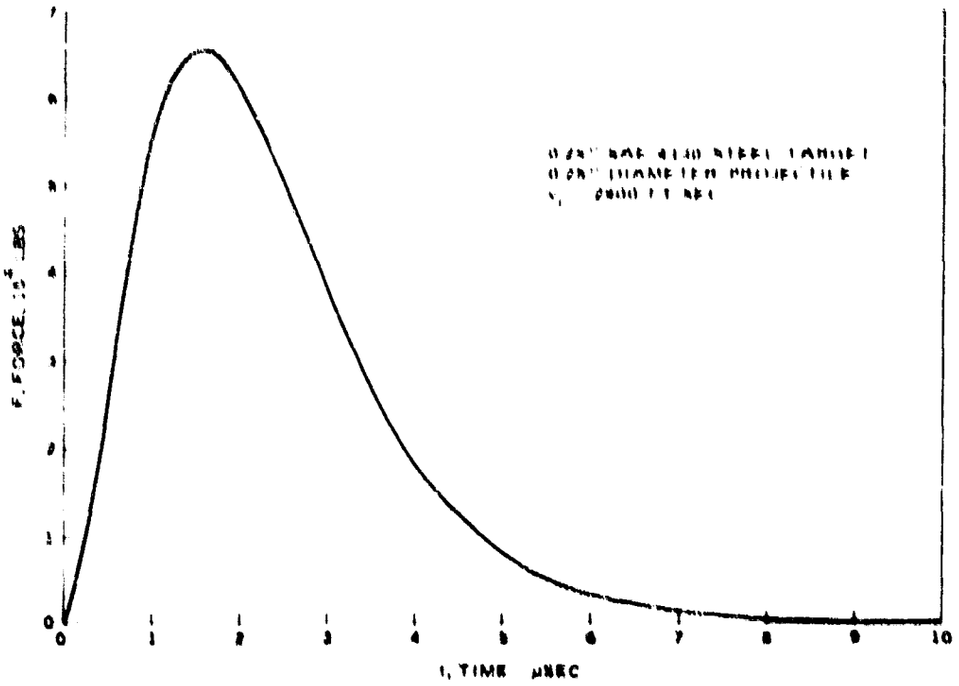

FIG. 26. Force-Time Curve for the Data Corresponding to Fig. 22.

from the last material in regions adjacent to the central crater at projectile velocities above about 5,500 fps. The limit of successful plug recovery was found to be about 7,000 fps for the 0.25-inch-thick steel targets, but considerably lower, of the order of 4,000 to 5,000 fps, when thin targets were employed.

At initial velocities of 8,600 fps, evidence of ring formation was noted in the 0.05-inch-thick 2024-T3 aluminum, whereas definite rings on the impact and the exit sides were observed in the 0.125-inch and 0.25-inch-thick aluminum and in the SAE 4130 target shown in Fig. 28. Rings were also found on the impact side of the 0.25-inch-thick fine-grained SAE 1020 steel plates; all are indicative of shear failure. However, the large rings punched out in the 0.25-inch-thick coarse-grained SAE 1020 steel plates were found to be largely the result of failure produced by tension rather than by shear.

The changing deformation pattern of the plate with increasing impact velocity described above, with a metamorphosis from dishing to punching, is supported by the information derived from the strain gages. The maximum symmetric strain in both thin and thick targets decreases by an average of about 65 percent from the peak to the minimum perforation velocity, whereas the corresponding maximum antisymmetric strain doubles

TABLE 2 Summary of Displacement, Velocity and Force Data and Comparison

						Measured velocity, fps				

placement, Velocity and Force Data and Comparison With Theoretical Results

Measured velocity, fps		Terminal velocity v_t^*, fps	Change in projectile momentum, Ans-lb-sec	Contact duration, msec[#]	Maximum force,[*] lb	Max force lb	Computer program results[†]				
Initial v_i	Terminal v_t						Terminal force, lb	Case Data			
								A	B	C	D
2900	Penetration		0.2145	1.15	41,800	42,650	2.5	2027.6	1.1.1.1	51.00	261.9
2900	Penetration		0.2108	8.4	50,200	65,450	1.5	1211.6	1.1.1.1	11.04	257.2
2850	2015	2608	0.0171	5.6	0.220	9.4.80	1.1	8.1.1	1.20.2	55.09	220.9
2800	2560	2480	0.0182	4.0	9.100	11.5.2	0.9	2.1.6	1.5.2.1	8.5.29	221.6
2800	2100	1080	0.0609	6.5	16,000	16,350	2.4	69.33	0.63289	61.36	216.5
2800	2.110	2182	0.1215	8.2	29,600	33,440	1.0	41.98	1.0.46	21.24	884.2
2850	2290	2000	0.4380	8.1	10,900	10,530	1.6	22.24	0.4192	6.1.37	210.3
2850	1600	1406	0.0882	10.1	10,100	20,250	1.6	1.1.1.9	0.9215	56.38	80.54
2965	2260	1940	0.1745								
3860	3.056	3006	0.1488								
4.110	3.288	2960	0.0744								
5008	4.430	3828	0.0808								
4806	710	1470	0.2998								
6940	2.866	2210	0.3324								
6022	688	1.118	0.3160								
7040	2148	2002	0.3680								
8170	2830	2421	0.3884								
8560	8000	7680	0.0400	1.8	44,400	49,860	0.6	.9876	1.198	57.89	27.10
8414	7905	7526	0.0386	1.8	42,800	44,276	0.7	7.285	0.2947	54.02	280.2
7860	7650	7282	0.0743	2.6	67,200	67,910	0.8	15.70	1.600	77.38	396.4
8766	6785	6000	0.1432	2.1	136,600	139,900	0.9	18.15	0.4080	47.21	270.6
7820	6720	6036	0.2726	2.8	194,800	226,360	0.8	62.40	1.594	72.56	351.1
8560	7300	6416	0.0900	2.7	67,300	78,690	0.8	66.34	1.466	76.03	300.0
8350	6230	4932	0.1642	4.6	67,000	87,180	1.4	208.8	1.590	108.0	347.8
7920	6820	5478	0.5205	5.6	189,200	213,280	1.6	181.3	1.378	121.5	469.3
8600	3000	2780	0.4070	5.8	140,000	141,870	2.5	200.5	0.4938	40.22	348.3
8650	2925	2606	0.4167	5.8	143,600	144,150	2.5	205.4	0.6379	44.89	182.3

TABLE 3. Mechanical Properties of Target Materials

Material	E Young's modulus[a] 10^6 psi	μ Poisson's ratio	σp Porportional limit[a] 10^3 psi	σu Ultimate strength[a] 10^3 psi	σs Ultimate strength 10^3 psi	Rockwell hardness
2024-O Aluminum	10.6	.33	12.8	34.0	19.0	H88
2024-T3 Aluminum	10.6	.33	53.0	70.0	41.9	B76
2024-T4 Aluminum	10.6	.33	53.0	69.2	41.9	B78
SAE 1020 Steel, large-grained	29.6	.29	64.0	71.0	45.2	B90
SAE 1020 Steel, small-grained	29.6	.29	48.0	59.5	37.9	B77
SAE 4130 Steel, quenched and tempered	29.6	.29	170.0	189.0	113.5	C40

[a] Quasistatic tension

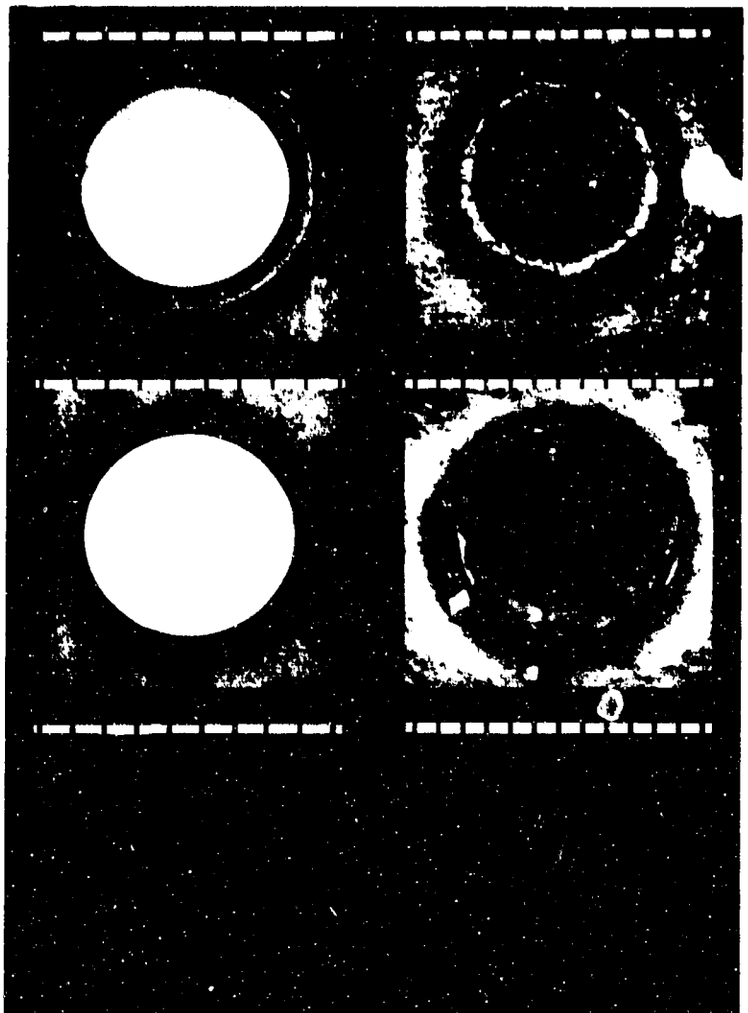

FIG. 27. Photographs (Top to Bottom) of the Impact and Exit Sides and Section of Targets. Perforation by 0.25-inch-diam. steel spheres travelling with an initial velocity of about 2,800 fps; the recovered plug is shown in the section view. (A) 0.062-inch-thick SAE 1020 steel target, and (B) 0.25-inch-thick 2024-T4 aluminum target. 1 mm scale.

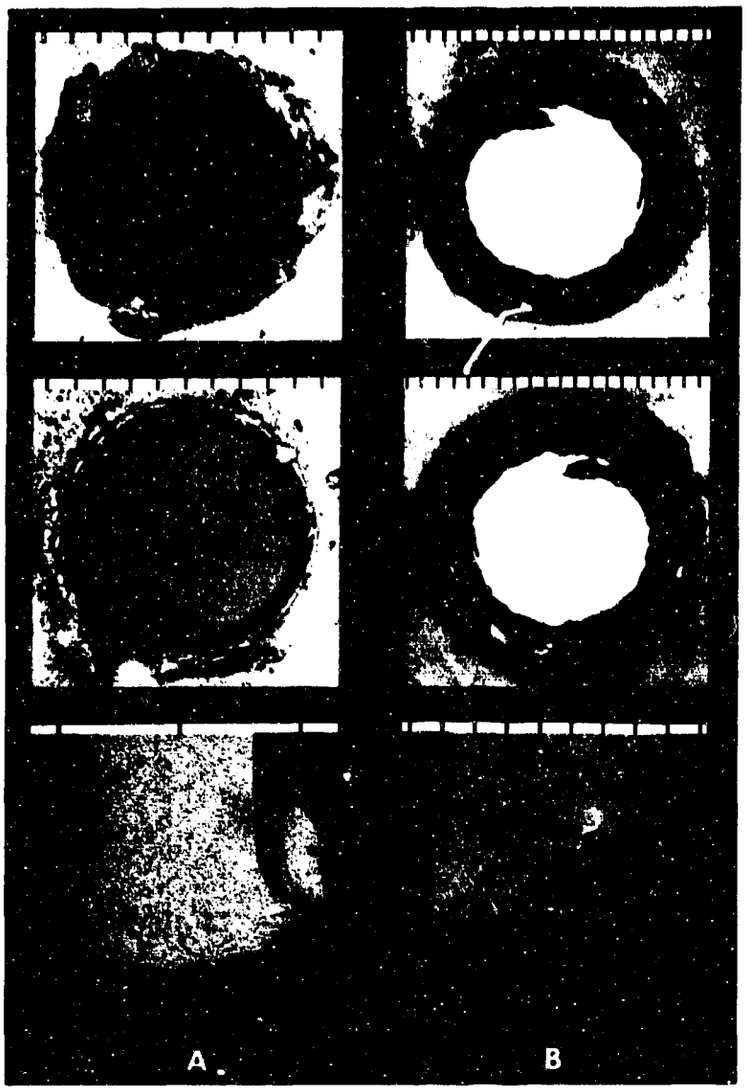

FIG. 28. Photographs (Top to Bottom) of the Impact and Exit Sides and Section of Targets. Perforation by 0.25-inch-diam. steel spheres travelling with an initial velocity of about 8,600 fps. (A) 0.05-inch-thick 2024-0 aluminum target, and (B) 0.25-inch-thick SAE 4130 steel target. 1 mm scale.

FIG. 29. Photographs of the Section of Penetrated Targets. The 0.25-inch-diameter steel spheres were travelling with an initial velocity of about 2,900 fps. (a) 0.25-inch-thick SAE 1020 steel, and (b) 0.25-inch-thick SAE 4130 steel. 1 mm scale.

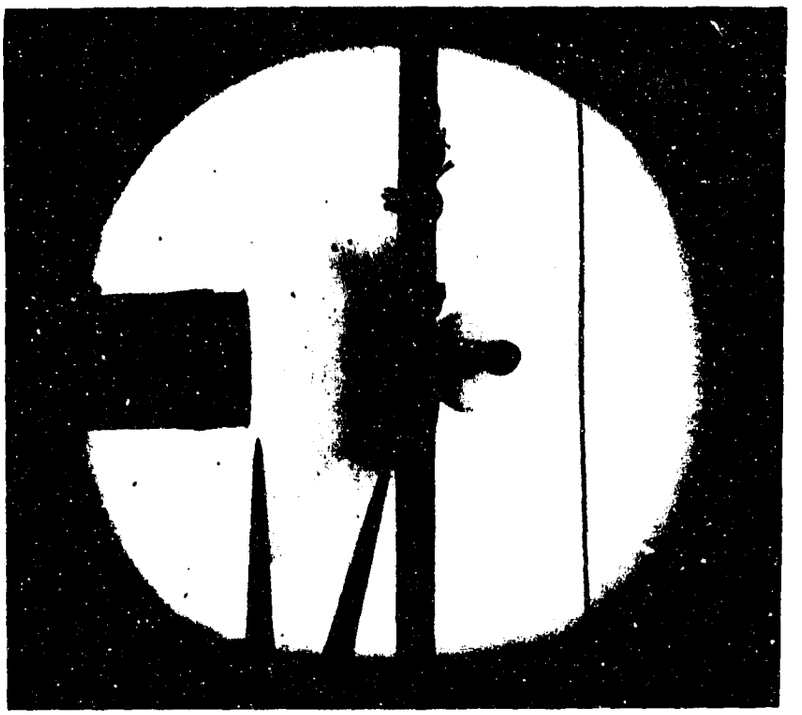

FIG. 30. Perforation Process. This photo shows a 0.25-inch-thick SAE 1020 steel plate 25 μsec after impact by a 0.25-inch-diameter steel sphere travelling with an initial velocity of 4,310 fps.

over this range. The last trend was also found in the perforation results quoted in Ref. 1. Thus, the radial motion of the target due to hole enlargement becomes more dominant with increasing velocity, while the effects of bending diminish, as would be expected. However, both of these components represent a completely negligible fraction of the initial kinetic energy of the projectile and can be ignored in an energy balance. For example, for an assumed half-sinusoidal component of symmetric elastic strain of amplitude ε_m and duration t_1 at position r relative to the impact point, the kinetic energy of the pulse is given by $T = E^2 r h_o t_1 / 2\rho c$ where h_o and c are the thickness and dilatational velocity of the plates, respectively. For the thin 2024-T3 aluminum plate struck at the high velocity, this yields a value of the order of 0.5 lb-in. The strain energy of this pulse as well as the energy contained in the antisymmetric transient are expected to be of the same magnitude or at most one order greater, whereas the initial energy of the projectile is 32,000 in-lb. The peak bending strain of 1,550 μin/in observed in this target during low velocity perforation compares with values of 2,000 to 3,000 μin/in recorded during the impact of a 0.5-inch-diameter steel sphere with an initial velocity ranging from 500 to 930

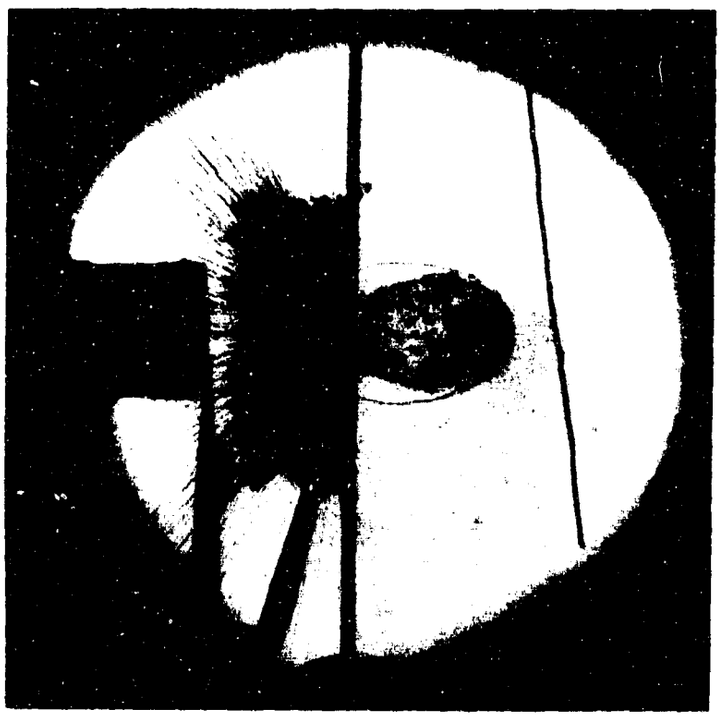

FIG. 31. Perforation Process. A 0.062-inch-thick SAE 1020 steel plate 25 μsec after impact by a 0.25-inch-diameter steel sphere travelling with an initial velocity of 8,600 fps.

fps at positions 1.5 to 3 inches from the contact point (Ref. 1). There is no exact method of calculating the amount of work required to produce a permanent deflection at the crater edge of 0.01 inch in the thin, soft aluminum target under the dynamic conditions of the low-velocity perforation. However, since a nonperforation run for a 0.25-inch-diameter projectile travelling at 550 fps and thus possessing an initial kinetic energy of 130.1 in-lb yielded a plate deflection at the center of 0.329 inch (Ref. 1), it must be presumed that the energy required to produce the present deformation is at least one order of magnitude lower than this, and thus of the order of 0.3 percent of the initial bullet energy at the present minimum velocity. Thus, for the range of velocities considered here, both elastic wave propagation and permanent deformation of the target under perforation conditions can be omitted in an energy balance.

The oscillations superposed on the strain gage records range from 200 to 600 kilohertz for the thin targets and from about 200 kilohertz to 2 megahertz for the thick targets. Dilatational waves successively

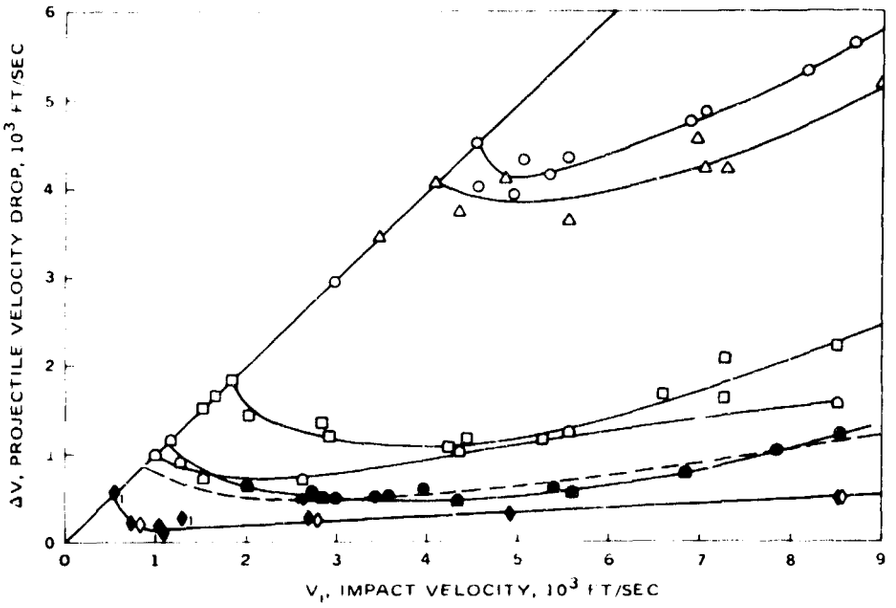

SYMBOL	TARGET	STEEL PROJECTILE DIAMETER
○	0.250 4130 STEEL ARMOR	0.250
△	0.250 1020 STEEL (LARGE GRAINED)	0.250
□	0.250 2024-T4 ALUMINUM	0.250
■	0.125 2024-T3 ALUMINUM	0.250
⌂	0.0625 1020 STEEL (SMALL GRAINED	0.250
●	0.0625 1020 STEEL (SMALL GRAINED)	0.375
◊	0.050 2024-T3 ALUMINUM	0.250
♦	0.050 2024-0 ALUMINUM	0.250
♦₁	FROM REF 1	

FIG. 32. Velocity Drop Through the Target as a Function of Initial Velocity for Several Impact Conditions.

reflecting from the two target surfaces would produce frequencies of 2 megahertz and 400 kilohertz for the 0.05-inch and 0.25-inch-thick targets, respectively and thus probably contribute to this effect, but cannot be considered as the complete cause of this effect. It is speculated that this phenomenon may be partly due to circuit ringing and to electromagnetic signals generated by the impact as observed by others.[2] The propagation velocity of the elastic bending pulse was found to be about 60,000 in/sec, whereas the plastic bending strain noted in Ref. 1 was observed to travel with a velocity of only 8,800 in/sec in the thin, soft aluminum target.

[2] S. Bodner. Personal communication.

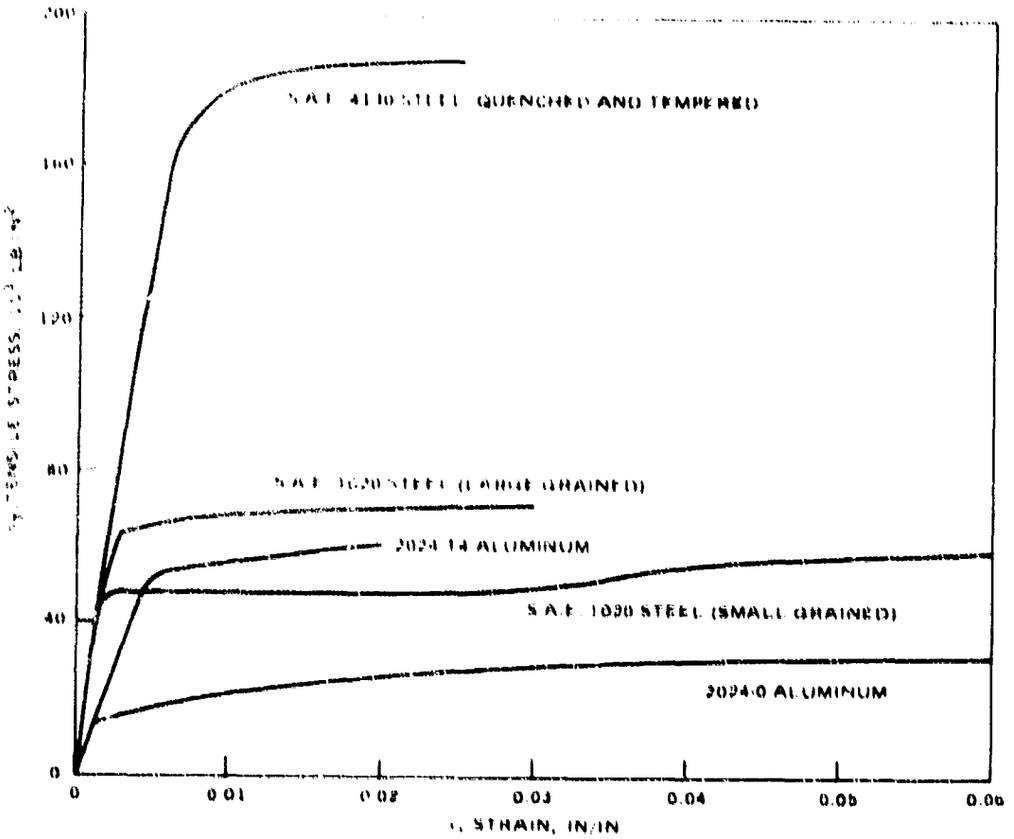

FIG. 33. Quasi-Static Tensile Stress-Strain Curves for Test Materials. (A) SAE 4130 steel, quenched and tempered, (B) SAE 1020 steel, large-grained, (C) SAE 1020 steel, small-grained, (D) 2024-T4 aluminum, and (E) 2024-0 aluminum.

With few exceptions, the inner crater diameter was found to increase with impact velocity, projectile diameter and, at the higher velocities, with target thickness. No significant increase was found in the crater diameter in the penetration tests with increase in initial velocity.

The terminal velocity of the projectile was generally obtained from the signals generated by the second velocity coil. This raised the question whether these voltages were produced jointly by the plug and the shattered projectile or by the plug alone, with the projectile travelling at a substantially lower speed. Examination of the recovered fragments indicated that the projectile and the plug were generally fused for initial velocities up to 7,000 fps so that no difference in the speeds of these two masses should exist. Beyond this range, there is a possibility that the terminal velocity of the projectile is less than that indicated, although presumably not by much. However, in the vicinity

of the ballistic limit, the perforation process appears to be somewhat erratic—particularly for the thick steels—accounting for the scatter in the velocity drop data for these materials shown near the limit of penetration in Fig. 32.

The change in the fragmentation pattern with increasing impact velocity is clearly illustrated in Fig. 30 and 31; in the first picture, with v_i = 4,310 fps, the plug and projectile still form a cohesive unit after perforation, whereas in the second photograph, with v_i = 8,600 fps, both plug and bullet have been virtually pulverized.

The variation of projectile velocity drop with initial speed shown in Fig. 32 indicates a decrease just beyond the ballistic limit, as predicted by the relation from Ref. 17,

$$v_f = \frac{m_o}{m_o+m_p} [v_i^2 - v_L^2]^{1/2} \qquad (7)$$

where m_o and m_p are the projectile and plug mass and v_i, v_f, and v_L the initial, terminal and ballistic limit projectile velocities, respectively. The authors of Eq. (7) acknowedge its applicability only in the vicinity of this limit; even here, the relation yielded a velocity drop 40 to 50 percent larger than observed in the perforation of a 0.05-inch-thick 2024-0 aluminum target by a 0.5-inch-diameter steel sphere (Ref. 1). As noted from the diagram, the velocity drop shortly thereafter begins to increase with projectile speed with the harder materials exhibiting a greater slope. This behavior cannot be explained by Eq. (7), but conforms to the pattern predicted by the relations derived in Ref. 23 and reproduced in Appendix A. Table 2 indicates the degree of correspondence between the measured and calculated terminal velocities; the greatest discrepancies are found in the intermediate velocity range and at the ballistic limit.

The projectile displacement histories portrayed in Fig. 16 through 22 were essentially constructed from the projectile velocity and fragment thickness data; the photographic information served only as auxiliary evidence. In general, a number of position-time diagrams were examined for a particular impact condition in order to ascertain the effect of slight variations in the location of the curve on the peak force evaluated from the empirical equations; this was found to be small when all the constraints were enforced. As noted in Table 2, these computed peak forces were in good general correspondence, although usually slightly higher than values of this parameter calculated on the basis of a triangular force pulse with the observed duration and an impulse equal to the measured change of projectile momentum. This indicates the absence of large spikes in the empirical force history, a general insensitivity of this relation to the detailed perforation process for a fixed duration of contact and prescribed initial and terminal projectile velocities, and the possibility of a reasonable peak force estimate from the triangular pulse shape. A more exact delineation of the actual force

history could be theoretically derived upon integration of Eq. (A-1) and (A-3) for the appropriate experimental conditions and comparison of the results with that given by Eq. (1) and (2) and the constants listed in Table 2.

In general, the peak force increased in magnitude with increased projectile speed, target strength, plate thickness, and projectile diameter, while the contact duration decreased with increasing v_i and increased with all the other parameters. The calculated values ranged from a magnitude of 9,430 lb with a rise time of 1.1 μsec and a duration of 5.5 μsec for the perforation of the 0.05-inch-thick 2024-0 aluminum by a 0.25-inch-diameter sphere travelling at 2,850 fps, involving a momentum change of 0.0171 lb-sec, to a value of 226,360 lb with a rise time of 0.8 μsec and τ = 2.8 μsec for a 0.375-inch-diameter sphere perforating a 0.062-inch-thick SAE 1020 steel target with an initial velocity of 7,820 fps, where Δmv = 0.2726 lb-sec. This compares with values of the peak force of 1,500 lb, rise times of 45 μsec and 20 μsec, and durations of 190 and 60 μsec calculated by the identical procedure for the perforation of a 0.05-inch-thick aluminum sheet by a 0.5-inch-diameter hard-steel sphere travelling at initial velocities of 493 and 933 fps, respectively. The corresponding changes of momentum for the two cases were found to be 0.109 and 0.040 lb-sec (Ref. 1). The peak forces derived from the present tests translate into pressures ranging from a minimum of 200,000 lb/in^2 to a maximum of 3 x 10^6 lb/in^2. While the smaller values of this pressure are distinctly within the proper domain of continuum theories of solid materials, the higher values approach the domain where hydrodynamic theories of perforation might be considered, such as given in Ref. 2. On the other hand, such theories are ordinarily regarded to apply in the hypervelocity impact regime above initial velocities of 10,000 fps where the effects of target and projectile compressibility become significant. Since the only evidence of the effect of thermodynamic (rather than mechanical) processes in the present experiments are the fusion of plug and projectile, and peak pressures act only for a fraction of a microsecond, the analysis of the observed phenomena should be accomplished by considering the projectile-target system as solids rather than as fluids. However, at higher impact velocities, where particulate jetting and vaporization effects manifest themselves, the masses should be treated as compressible fluids and shock propagation should be analyzed by means of the Rankine-Hugoniot relations.

CONCLUSIONS

From an experimental investigation of the perforation of thin targets composed of aluminum and steel and the penetration and perforation of thicker plates of the same material by hard-steel projectiles with diameters of 0.125-, 0.25-, and 0.375-inch in the initial velocity range from 2,800 to 8,800 fps, it is concluded that:

(1) The velocity drop in the projectile decreases from the ballistic limit to a minimum value and then increases monotonously with initial velocity for all projectile-target combinations.

(2) Slight dishing observed in the thin targets at low velocities disappears at higher projectile speeds with the perforation mechanism converted to a punching operation. This is supported by strain gage results that show the relative increase of radial plate motion relative to bending effects with increasing bullet velocity.

(3) Plug recovery is limited to impact speeds of 4,000 to 5,000 fps for metallic targets of thickness in the range of 0.05 inch and to velocities of 7,000 fps for 0.25-inch-thick targets.

(4) The inner crater diameter increased in size with initial velocity and projectile diameter and, at higher velocities, with target thickness.

(5) Terminal plug and projectile velocities are substantially identical.

(6) The observed phenomena are in conformity with those prevailing at lower impact velocities in identical targets noted in previous investigations. However, the present velocity range introduces the element of fragmentation not found in earlier tests.

(7) Significant errors accrue in the calculation of the terminal velocity based on a momentum balance of plug and projectile, but much better correlation is obtained with predicted results from a theory accounting for target compression, shear, and inertial resistance.

(8) Displacement histories of the projectile can be constructed from the measured initial and terminal velocity of the projectile and the plug thickness without the need of a framing camera. Small variations in such curves (but with observation of the above constraints) did not significantly affect the magnitude of the peak force computed from these data by means of an empirical relation. These peak forces were generally higher, but agreed well with corresponding values computed from an assumed triangular impulse of proper duration and magnitude.

(9) The pressures developed in the projectile-target system are of sufficiently low magnitude and duration so that the analysis of the perforation process can be performed by considering the participating bodies as solids rather than as compressible fluids.

Appendix

PERFORATION OF METALLIC PLATES BY A PROJECTILE

Analysis of the perforation of metallic plates by a projectile according to J. Awerbuch (Ref. 23) is recapped here, as the original publication may not be readily available.

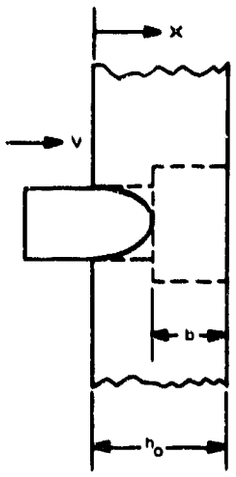

FIG. 34.
Penetration

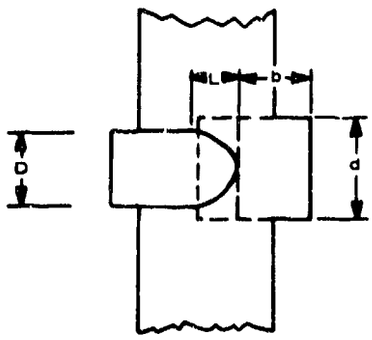

FIG. 35.
Plugging

PENETRATION

Equation of Motion

$$-F_i - F_c = -\frac{1}{2}\rho\, KAv^2 - \sigma_u A = \frac{d}{dt}(mv) = \frac{d}{dt}(m_o + \rho\, Ax)v + m\frac{dv}{dt}$$

$$= \rho\, Av^2 + (m_o + \rho\, Ax)v\frac{dv}{dx} \qquad \text{(A-1)}$$

$$v_b = \left[\left(v_i^2 + \frac{\sigma_u}{\rho\left\{1 + \frac{1}{2}K\right\}}\right)\left(\frac{m_o/\rho A}{h_o - b + \frac{m_o}{\rho A}}\right)^{[2+K]} - \frac{\sigma_u}{\rho\left\{1 + \frac{1}{2}K\right\}}\right]^{1/2} \qquad \text{(A-2)}$$

PLUGGING

Equation of Motion

$$\tau\, dbt_f = [m_o + \rho A(h_o - b)]v_b - [m_o + \rho Ab + \rho A(h_o - b)]v_f \qquad \text{(A-3)}$$

$$v_f = \frac{-m_p v_b + \sqrt{(m_p v_b)^2 + 4(m_o + \rho Ah_o)(C_1 v_b^2 - C_2)}}{2(m_o + \rho Ah_o)} \qquad \text{(A-4)}$$

where $m_p = \rho Ab$ = Plug mass, and

$C_1 = m_o + \rho A(h_o - b)$

$C_2 = 2\pi db^2\sigma_s$

NOMENCLATURE

A Projected area of bullet nose

b Plug width

D Projectile diameter

d Plug diameter

F_i Inertial resistance of target material during penetration = $\frac{1}{2}\rho\ KAv^2$

F_c Compressive resistance of target during penetration = $\sigma_u A$

F_s Resisting shear force of target during plugging = $\sigma_s \pi\ db$

h_o Target thickness

K Numerical constant depending on projectile nose geometry

= 1 for a cylinder = 1/2 for a sphere, and

$$= 1 + \frac{16L^2}{\pi^2 D^2}\ Ln\ \frac{16L^2}{\pi^2 D^2 + 16L^2}$$ for an ogival nose

m Effective projectile mass (during penetration) = $m_o + \rho Ax$

m_o Initial projectile mass

ρ Target mass density

t_p Duration of plugging phase, assumed to occur under constant deceleration

σ_u Ultimate compressive strength

σ_s Ultimate shear strength

v Velocity

v_i Initial projectile velocity

v_b Velocity at end of penetration

v_f Velocity at end of plugging (perforation)

x Coordinate along direction of perforation

REFERENCES

1. Calder, C. A. "Plastic Deformation and Perforation of Thin Plates Resulting from Projectile Impact," Dissertation (PhD), University of California, Berkeley, 1969.

2. GM Defense Research Laboratories. *Final Report on Investigation of Fundamental Mechanism of Damage to Thin Targets by Hypervelocity Projectiles*, by C. J. Maiden, J. W. Gehring, and A. R. McMillan. Santa Barbara, Calif., September, 1963. Contract No. 3891(00)(X), (NRL TR63-225).

3. Cook, M. A. "Mechanism of Cratering in High-Velocity Impact," J APPL PHYS, Vol. 20, (1959), p. 725.

4. Boussinesq, J. *Applications des potentiels à l'étude de l'équilibre et du mouvement des solides élastiques.* Paris, Gauthier-Villars, 1885.

5. Goldsmith, W., T. W. Liu, and S. J. Chulay. "Plate Impact and Perforation by Projectiles," EXP MECH, Vol. 5, No. 12, (1965), p. 385.

6. Karas, K. "Platten unter seitlichem Stoss," ING ARCH, Vol. 10, (1939), p. 237.

7. Zener, C. "The Intrinsic Inelasticity of Large Plates," PHYS REV, Vol. 59, (1941), p. 669.

8. Hopkins, H. G. *On the Impact Loading of Circular Plates Made of Ductile Metal,* Division of Applied Mechanics, Brown University. (Report No. DA-2598/7, AD 22938), 1953.

9. Chulay, S. J. "Dynamic Behavior of Plastic Plates," Dissertation (PhD), University of California, Berkeley, 1966.

10. Kelly, J. M. and T. Wierzbicki. "Motion of a Circular Viscoplastic Plate Subject of Projectile Impact," Z ANGEW MATH U PHYS, Vol. 18, (1967), p. 236.

11. Wierzbicki, T. "Impulsive Loading of Rigid Viscoplastic Plates," INT J SOLIDS STRUC, Vol. 3, (1967), p. 635.

12. Wierzbicki, T. and J. M. Kelly. "Finite Deflection of a Circular Viscoplastic Plate Subject to Projectile Impact," INT J SOLIDS STRUC, Vol. 4, (1968), p. 1081.

13. Rinehart, J. S. and J. Pearson. *Behavior of Metals Under Impulsive Loads.* Dover Publications, New York, 1965.

14. Taylor, G. I. "The Formation and Enlargement of a Circular Hole in a Thin, Plastic Sheet," QUART J MECH APPL MATH, Vol. 1, (1948), p. 103.

15. Freiberger, W. "A Problem in Dynamic Plasticity: The Enlargement of a Circular Hole in a Flat Sheet," CAMBRIDGE PHIL SOC, PROC, MATH PHYS SCI, Vol. 48, (1952), p. 135.

16. Thomsen, W. T. "An Approximate Theory of Armor Penetration," J APPL PHYS, Vol. 26, (1955), p. 80.

17. Recht, R. F. and R. W. Ipson. "Ballistic Perforation Dynamics," J APPL MECH, Vol. 30, (1963), p. 384.

18. Zaid, M. and B. Paul. "Mechanics of High Speed Projectile Perforation," FRANKLIN INST J, Vol. 264, (1957), p. 117.

19. Zaid, M. and B. Paul. "Armor Penetration," ORDNANCE, Vol. 41, (1957), p. 609.

20. Zaid, M. and B. Paul. "Normal Perforation of a Thin Plate by Truncated Projectiles," FRANKLIN INST J, Vol. 265, (1958), p. 317.

21. Pytel, A. and N. Davids. "A Viscous Model for Plug Formation in Plates," FRANKLIN INST J, Vol. 276, (1963), p. 394.

22. Chou, I. C. "Viscoplastic Flow Theory in Hypervelocity Perforation of Plates," Proceedings of the Fifth Symposium on Hypervelocity Impact, Vol. 1, (1962), p. 307.

23. Awerbuch, J. "A Mechanics Approach to Projectile Penetration," Thesis (MS), TECHNION (Haifa, Israel), 1970.

24. Goldsmith, W. *Impact*. London, Edward Arnold, 1960.

25. U. S. Naval Ordnance Test Station. *Impact at Intermediate Velocities Involving Contact Phenomena,* by W. Goldsmith. China Lake, Calif., NOTS, 1963. (NOTS TP 3125.)

26. Spells, K. E. "Velocities of Steel Fragments After Perforation of Steel Plates," PHYS SOC LONDON, PROC, SER B, Vol. 64, (1951), p. 212.

27. Clark, A. B. J., W. F. Hassel, and J. M. Krafft. *The Penetration of Thin 2-S Aluminum Sheets by Rocket Models,* Naval Research Laboratory, Washington, D. C., (May 1959), Report 150.

28. Krafft, J. M. "Surface Friction in Ballistic Penetration," J APPL PHYS, Vol. 26, No. 10, (1955), p. 1248.

29. Bluhm, J. I. "Stresses in Projectiles During Penetration," SOC EXP STRESS ANAL, PROC, Vol. 13, No. 2, (1956), p. 167.

30. Masket, A. V. "The Measurement of Forces Resisting Armor Penetration," J APPL PHYS, Vol. 20, (1949), p. 132.

31. Medick, M. A. "On Classical Plate Theory and Wave Propagation," J APPL MECH, Vol. 28, No. 2, AMER SOC MECH ENG, TRANS: SER E, (1961), p. 223.

32. Allen, W. A., G. E. Meloy, and J. W. Rogers. "Hypervelocity Precision Impact Instrument," REV SCI INSTRUM, Vol. 31, No. 7, (1960), p. 726.

33. Calder, C. A. "A Simple, Inexpensive Projectile Velocity Gauge," J SCI INSTRU, Vol. 1, (1968), p. 882.

34. Naval Weapons Center. *Use of a Kerr Cell Camera in the Study of Perforation Mechanics* (U), by S. A. Finnegan and K. I. Rinehart. Transactions of the Fifth NWC Warhead Research and Development Symposium, China Lake, Calif., NWC, December 1967. (NWC TP 4446, Vol. 2, publication CONFIDENTIAL.)

35. Goldsmith, W. and P. T. Lyman. "The Penetration of Hard-Steel Spheres Into Plane Metal Surfaces, J APPL MECH, Vol. 27, AMER SOC MECH ENG, TRANS: SER E, (1960), p. 717.

36. Naval Weapons Center. *Multiflash Lighting System for High-Speed Shadowgraph Photography* (U), by Kenneth I. Rinehart. Transactions of the Sixth NWC Warhead Research and Development Symposium, China Lake, Calif., NWC, October 1969. (NWC TP 4835, Vol. 2, publication CONFIDENTIAL.)

ACKNOWLEDGEMENT

The authors would like to express their appreciation to Mr. Roland Kenner of the University of California, Berkeley, and to Mr. Fred Hallsthammer, Naval Weapons Center, for computational assistance.